



HAL
open science

Depositional Setting of Algoma-type Banded Iron Formation

Blandine Gourcerol, P C Thurston, D J Kontak, O Côté-Mantha, J Biczok

► **To cite this version:**

Blandine Gourcerol, P C Thurston, D J Kontak, O Côté-Mantha, J Biczok. Depositional Setting of Algoma-type Banded Iron Formation. Precambrian Research, 2016. hal-02283951

HAL Id: hal-02283951

<https://brgm.hal.science/hal-02283951>

Submitted on 11 Sep 2019

HAL is a multi-disciplinary open access archive for the deposit and dissemination of scientific research documents, whether they are published or not. The documents may come from teaching and research institutions in France or abroad, or from public or private research centers.

L'archive ouverte pluridisciplinaire **HAL**, est destinée au dépôt et à la diffusion de documents scientifiques de niveau recherche, publiés ou non, émanant des établissements d'enseignement et de recherche français ou étrangers, des laboratoires publics ou privés.

Accepted Manuscript

Depositional Setting of Algoma-type Banded Iron Formation

B. Gourcerol, P.C. Thurston, D.J. Kontak, O. Côté-Mantha, J. Biczok

PII: S0301-9268(16)30108-5

DOI: <http://dx.doi.org/10.1016/j.precamres.2016.04.019>

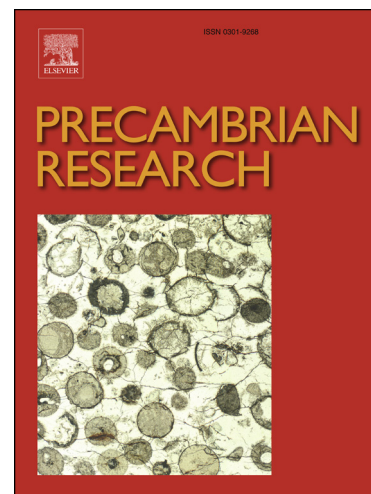
Reference: PRECAM 4501

To appear in: *Precambrian Research*

Received Date: 26 September 2015

Revised Date: 21 January 2016

Accepted Date: 30 April 2016



Please cite this article as: B. Gourcerol, P.C. Thurston, D.J. Kontak, O. Côté-Mantha, J. Biczok, Depositional Setting of Algoma-type Banded Iron Formation, *Precambrian Research* (2016), doi: <http://dx.doi.org/10.1016/j.precamres.2016.04.019>

This is a PDF file of an unedited manuscript that has been accepted for publication. As a service to our customers we are providing this early version of the manuscript. The manuscript will undergo copyediting, typesetting, and review of the resulting proof before it is published in its final form. Please note that during the production process errors may be discovered which could affect the content, and all legal disclaimers that apply to the journal pertain.

Title: Depositional Setting of Algoma-type Banded Iron Formation.**B. Gourcerol¹, P.C. Thurston¹, D.J. Kontak¹, O. Côté-Mantha² and J. Biczok³**

¹ Mineral Exploration Research Centre, Laurentian University, Sudbury, Ontario, Canada P3E 2C6

² AgnicoEagle Mines Ltd – Division Exploration, 765 Chemin de la mine Goldex, Val d'Or, Québec, Canada J9P 4N9

³ Consulting geologist, Greely, Ontario, Canada

***Corresponding author:** Blandine Gourcerol; Email: gourcerol.blandine@gmail.com

1. Abstract

Algoma-type banded iron formations (BIF) are chemical sedimentary rocks characterized by alternating layers of iron-rich minerals and chert that are generally interstratified with bimodal submarine volcanic rocks and/or sedimentary sequences in Archean greenstone belts. However, the geological setting for Algoma-type BIF deposition remains equivocal due to the effects of post-depositional deformation and metamorphism and absence of modern analogues for comparative studies. It is commonly accepted that the abundance of rare earth element and yttrium (REE+Y) in chert bands may retain a primary geochemical signature and therefore constrain their geological setting. In order to explore the latter, a geochemical study using the laser ablation-inductively coupled plasma-mass spectrometry (LA-ICP-MS) methodology was done using cherts from four Canadian BIF-hosted gold deposits. These results suggest that chert bands record: (1) interaction of seawater with Fe-oxyhydroxides, as suggested by their heavy

REE enrichment coupled with La and Y enrichments; (2) contributions from high-temperature (>250°C) hydrothermal fluids, as suggested by positive Eu excursions; and (3) detrital contamination, which is suggested by relatively consistent REE concentrations and a chondritic Y/Ho ratio (i.e., $Y/Ho \approx 27$). Water-column pH conditions at the time of BIF deposition are evaluated using Ce/Ce*: a positive Ce/Ce* anomaly suggests relatively acidic conditions (i.e., $pH \leq 5$) for most of the chert samples, but more alkaline conditions (i.e., $pH \geq 5$) for samples showing Fe-oxyhydroxide precipitation within chert bands. Finally, *in situ* using secondary ion mass spectrometry (SIMS) analysis ($n=73$) of chert from Meliadine show the $\delta^{18}O$ of primary amorphous silica (+27‰) was modified to values of around +8 to +20‰ during diagenesis at temperatures >100°C with a fluid having $\delta^{18}O_{H_2O} = 0$ to 5‰. Thus, whereas there has been O isotopic exchange during diagenesis, the REEs and trace elements are not modified in the chert due to the low concentrations of these elements in the reacting fluid of sea water origin.

Keywords: Banded iron formation, chert, geochemistry, deposition, seawater, oxygen isotope

2. Introduction

Algoma-type BIFs are thinly bedded, chemical sedimentary rocks comprising alternating layers of iron-rich minerals and chert. These rocks are typically intercalated with Eoarchean to late Paleoproterozoic volcano-sedimentary sequences within greenstone belts (Goodwin, 1973; Bekker et al., 2010). They differ from Superior-type BIFs which represent extensive units, mainly Proterozoic in age, located in passive margin sedimentary successions and showing no specific association with volcanic units (e.g., Gross, 1980; Bekker et al., 2010). Based on their sedimentary and geochemical features, a restricted basin model, equivalent to the modern Red

Sea, corresponding to closed to semi-closed basins where volcanic and hydrothermal activities were extensive represents one potential BIF depositional model (e.g., Barrett et al., 1988a; Bolhar et al., 2005; Ohmoto et al., 2006; Bekker et al., 2010). In this scenario, iron-rich minerals precipitated contemporaneously with hydrothermal vent fluids to form various iron oxyhydroxides, such as ferrihydrite. These primary minerals were subsequently transformed during diagenesis to hematite, magnetite and siderite depending in part on the microbial biomass concentration (Posth et al., 2013). Where metamorphosed, the Fe-rich assemblage may comprise more complex mineral assemblages that include a variety of silicate phases (e.g., amphibole, garnet, and plagioclase). The interbedded chert horizons are considered to reflect: (1) direct seawater precipitation (e.g., Bolhar et al., 2005; Thurston et al., 2012); (2) hydrothermal precipitation from vent fluids (Allwood et al., 2010; Thurston et al., 2012); and/or (3) the products of secondary replacement (Hanor and Duchac, 1990) as confirmed by their shale-normalized chemical signature (e.g., Thurston et al., 2011; Gourcerol et al., 2015a).

In this study, we explore the chert geochemistry at four Canadian BIF-hosted gold deposits (the ~4 Moz Au Meadowbank deposit, hosted by the 2.71 Ga Woodburn Lake greenstone belt; the ≥ 2.8 Moz Au Meliadine district, hosted by the 2.6 Ga Rankin Inlet greenstone belt; the ~6 Moz Au Musselwhite deposit, hosted by the 2.9-3 Ga North Caribou greenstone belt; and the ~4 Moz Au Beardmore Geraldton district, hosted by the 2.7 Ga eponymous greenstone belt) that are either intercalated with mafic to ultramafic volcanic rocks or associated interflow sediments. These four gold deposits were selected in order to validate the restricted-basin model (e.g., Barrett et al., 1988a) as a depositional setting for Algoma-type BIFs by using the geochemical signature of the chert bands as a proxy for the primary signature of ocean water chemistry and hydrothermal vent fluids. The chert chemistry was characterized by using *in situ* LA-ICP-MS

analysis following the protocol outlined in our earlier contributions (Gourcerol et al., 2015a, b). In addition, we have also analyzed the cherts *in situ* using secondary ion mass spectrometry (SIMS) to determine their $\delta^{18}\text{O}$ signature in order to assess their post depositional exchange with later fluids (e.g., diagenetic, metamorphic). As far as we are aware, this is the first study that integrates these two data sets, that is chert trace element chemistry, in particular the rare earth elements (REEs), and $\delta^{18}\text{O}$. An indirect intent of this study was also to examine if chert beds in these settings retain a geochemical signature that may relate to the gold mineralizing event. In detail, these hypotheses were tested by: (1) defining the role of chemical reservoirs (i.e., seawater, hydrothermal fluids, and terrestrial detritus) in chert deposition; and (2) using redox-sensitive REE+Y to assess the oxygenation state of the water column during chert precipitation.

3. Geological setting of the selected BIFs

3.1. The Meadowbank deposit

Located in the Rae Domain of the Churchill Province, the Meadowbank deposit is hosted by the Woodburn Lake greenstone belt (ca. 2.71 Ga), which consists of tholeiitic and komatiitic metavolcanic rocks with minor calc-alkaline felsic tuffs and flows with intercalated BIF and clastic metasedimentary rocks (Armitage et al., 1996; Sherlock et al., 2001a, b, 2004; Hrabí et al., 2003; Pehrsson et al., 2004). The regional metamorphic grade ranges from middle greenschist to amphibolite facies (Pehrsson et al., 2004) and the sequence was deformed by at least six regional-scale deformation events (e.g., Pehrsson et al., 2013; Janvier et al., 2015).

Numerous units of oxide-, silicate- and locally sulfide-facies Algoma-type BIF have been identified, which include the West IF, Central BIF and East BIF; all of the BIFs are generally interlayered with ultramafic to felsic volcanic rocks and locally with a quartzite unit (Gourcerol

et al., 2015a; Sherlock et al., 2001a, b, 2004). The BIF display cm- to mm-thick, laminated magnetite and white- to grey chert with associated layers (0.2 to 5 cm thick) of grunerite/biotite, cummingtonite/biotite or garnet/biotite combinations that are related to metamorphic variation on the property (e.g., Gourcerol et al., 2015a). Moreover, minor chlorite, sericite, ankerite, siderite, stilpnomelane and apatite grains are observed either as layers interbedded with chert and magnetite or as inclusions in chert bands (Armitage et al., 1996; Hrabí et al., 2003; Sherlock et al., 2004; Gourcerol et al., 2015a). These BIFs are described more in detail in Gourcerol et al. (2015a).

3.2. The Meliadine gold district

The Meliadine deposit is hosted by the 2.6 to 2.7 Ga Rankin Inlet greenstone belt (Wright, 1967; Aspler and Chiarenzelli, 1996a), which lies along the boundary between the Central and the North Western Hearne domains of the Churchill Province (Tella et al., 2007; Davis et al., 2008). The Rankin Inlet greenstone belt consists of polydeformed massive and pillowed mafic volcanic rocks, felsic pyroclastic rocks and associated interflow sedimentary units, gabbro sills and oxide-facies BIFs; all of these units are intruded by minor granite, undeformed biotite lamprophyre, as well as late gabbro and diabase dykes of Archean and Proterozoic age. These rocks have been metamorphosed from lower greenschist to lower-middle amphibolite facies (Carpenter, 2004; Carpenter, et al., 2005; Lawley et al., 2015).

Several Algoma-type BIFs are recognized along the structural hanging wall of the regional-scale Pyke Fault, including the Pump, F-Zone and Discovery (e.g., Lawley et al., 2015). These BIFs consist of continuous, subparallel, medium-grey cherty beds interbedded with

massive, mm- to cm-thick beds of magnetite BIF with some chert-grunerite units and local sulfide-facies. Minor cm- to mm-thick layers of chlorite are reported mainly in the Discovery BIF.

3.3. The Musselwhite deposit

Located in the North Caribou terrane of the Superior Province, the Musselwhite deposit is hosted by the North Caribou greenstone belt dominated by mafic to ultramafic metavolcanic rocks of the 2973 to <2967 Ma Opapimiskan-Markop metavolcanic assemblage and tholeiitic basalts and minor felsic volcanics of the 2980 to 2982 Ma South Rim metavolcanic assemblage (Biczok et al., 2012; McNicoll et al., 2013). These rocks have been metamorphosed from lower greenschist to lower-mid amphibolite facies (Breaks et al., 2001) and deformed by three deformation events (e.g., Hall and Rigg, 1986; Breaks et al., 2001; Oswald et al., 2015; McNicoll et al., 2016). The Opapimiskan-Markop metavolcanic assemblage consists, from the structural base to the top, of the “Lower Basalt” unit, the Southern Iron Formation, “Basement Basalt” unit and the Northern Iron Formation (Otto, 2002; Moran, 2008; Biczok et al., 2012).

The “Basement Basalt” unit is a thick sequence of massive- and pillowed tholeiitic basalt (Moran, 2008). The “Lower Basalt” unit is composed of basalt and ultramafic rocks, but includes extensive andesite (Hollings and Kerrich, 1999; Otto, 2002). The North Iron Formation is subdivided, from the structural base to top, into: pyrrhotite-rich mudstone (4H), chert-grunerite (4A), chert-magnetite (4B), clastic-chert-magnetite (“clastic”4B), garnet-grunerite-chert (4EA), garnetiferous amphibolite (4E) and garnet-biotite schist (4F) (e.g., Otto, 2002; Moran, 2008; Biczok et al., 2012). The Southern Iron Formation consists of two sub-parallel BIF horizons (Biczok et al., 2012). These BIFs are described more in detail in Gourcerol et al. (2015b).

3.4. The Beardmore Geraldton gold district

The Beardmore Geraldton gold district is hosted by the 2.7 Ga Beardmore-Geraldton Greenstone Belt located (BGGB) within the southern margin of the Wabigoon Subprovince (Lafrance et al., 2004). The BGGB consists of three east-trending shear-bounded units of metasedimentary and metavolcanic rocks. The southern assemblage is characterized by massive and pillowed basalt and andesite with thin sedimentary and tuffaceous beds (Shanks, 1993; Tomlinson et al., 1996) interbedded with wacke, conglomerate, siltstone and oxide-facies BIF in which the presence of jasper is notable. The central assemblage reflects felsic to mafic calc-alkaline and tholeiitic volcanic units that are associated with feldspathic sandstone, siltstone, argillite and minor BIF overlain by polymictic conglomerate (Lafrance et al., 2004). The occurrence of the pyroclastic rocks and large amygdules in the volcanic rocks suggest shallow-water or subaerial volcanism (Kresz and Zayachivsky, 1991). Lastly, the northern assemblage consists of massive and amygdaloidal pillowed tholeiitic basalt and andesite interbedded with polymictic conglomerate and minor sandstone (e.g., Mackasey et al., 1976). These rocks have been metamorphosed to greenschist facies and deformed by four events of deformation (Tóth et al., 2015).

The BIFs occur high in the stratigraphy of the southern metasedimentary belt and can be divided into three types (Fralick and Pufahl, 2006): (1) an iron oxide-rich type referred to as “a-type” which is a dominantly iron oxide-rich (i.e., magnetite and/or hematite) sediment interbedded with mm- to cm-scale graded or ungraded siltstone; (2) a siltstone-rich type (i.e., “b-type”) which is characterized by cm-scale graded to sharply bounded siltstone layers separated by mm-thick iron oxide-rich laminae; and (3) a sandstone-rich type (i.e., “c-type”) which

corresponds to sandstone beds separated by mm- to cm-scale iron oxide-rich bands. Hematitic chert laminae or bands (i.e., jasper) are common in the three types of BIF and are interbedded with either sediments or iron oxide-rich layers.

A braided fluvial system was proposed as the depositional environment for these BIFs (e.g., Barrett and Fralick 1989; Fralick and Pufahl, 2006) in which the BIFs occur mainly on flooding surfaces separating the offshore and the fluvial systems. The BIF and iron oxide-rich material were deposited during transgression whereas the interbedded siliciclastic sedimentary rocks reflect regression.

4. Analytical methods and data treatment

The BIF samples collected for this study included: (1) thirty-three samples from drill core and outcrops (Fig. 1A) from the Meadowbank deposit (i.e., West IF, Central BIF, East BIF); (2) forty samples in the Meliadine district (i.e., Pump, F-Zone and Discovery); (3) twenty-three samples from the Musselwhite deposit (i.e., chert-magnetite (4B), garnet-grunerite-(chert) (4EA), garnetiferous amphibolite (4E), and garnet-biotite schist (4F) facies); and (4) twenty seven samples from the Beardmore Geraldton district (i.e., a-, b- and c-types BIF).

4.1. Scanning electron microscopy and *in situ* LA-ICP-MS analysis

The chert material was analyzed by micro-sampling using laser ablation followed by ICP-MS analysis. The advantage of this protocol over bulk analysis is that it excludes any influence of later veining, sulfides or deformation-related metamorphic recrystallization-precipitation (e.g., Kamber and Webb, 2007). In order to select areas for analysis, polished thin sections (100 μm thick; Fig. 1B) were prepared and examined, using both transmitted and reflected light

microscopy; and selected material was studied in more detail using the scanning electron microscopy (SEM) coupled with an energy dispersive spectrometer (EDS) to select the most suitable chert bands with minimal amounts of detrital mineral inclusions and other contaminants related to alteration, diagenesis, metamorphic or ore-forming events (e.g., clastic grains, volcanic ash, phosphates). The SEM used was a JEOL 6400 SEM with an INCA energy dispersive spectrometer (EDS) system housed in the Central Analytical Facilities (CAF) at Laurentian University, Sudbury, Ontario. Operating conditions were accelerating voltage of 20 keV, 1.005 nA beam current, acquisition count times of 10 seconds, and a working distance of 15 mm.

The trace element chemistry was determined using a Thermo Scientific XSERIES II ICP-MS in a two-volume Laurin Technic sample cell using a pulsed ArF excimer laser (RESOLUTION M-50) emitting at 193 nm and a repetition rate of 10 Hz. The instrument operated with a forward power of 1450 W. Gas flows were 800 ml/min for argon, 650 ml/min for He and 6 ml/min for N₂. Dwell times for elements analysed were 10 ms. As chert bands have very low concentration of REEs, spot analyses may be below the limit of detection for many elements, hence, in order to circumvent this issue, line traverses using both 140 and 190 μm beam diameters were made with a repetition rate of 10 Hz and an energy density of 7 J/cm² (Fig. 1C). No pre-ablation was done as virtually any non microcrystalline quartz present would substantially modify the REE+Y patterns from their primary abundances. However, as the line traverse method increases the influence of any detrital contaminants, either as inclusions or minerals disseminated along the traverse line, the Queensland alluvial shale composite (MUQ) was used to normalize the REE+Y values to minimize the influence of potential terrigenous input. The MUQ composition represents a mixed bimodal felsic and mafic volcanic provenance (Kamber et al., 2005), which

acts as a proxy for the expected average terrigenous input from a typical bimodal greenstone belt into the Archean ocean (e.g., Bolhar et al., 2005; Thurston et al., 2012).

The elemental concentrations reported in this study (Tables 1, 2, 3 and 4) represent the integrated signal over the length of the line traverses, which measured about 6500 μm . The element list used for each analysis included the 14 REEs (La, Ce, Pr, Nd, Sm, Eu, Gd, Tb, Dy, Ho, Er, Tm, Yb and Lu), in addition to Li, Be, Si, Sc, Ti, V, Cr, Mn, Fe, Co, Ni, Cu, Zn, Ga, As, Rb, Sr, Y, Zr, Nb, Mo, Ag, Cd, In, Sn, Sb, Cs, Ba, Hf, Ta, W, Tl, Pb, Th and U. The detection limits for the analyzed elements vary based on a variety of factors, such as the volume of inclusions within chert. The detection limits were calculated using the relationship described in Longerich et al. (1996) and range from 0.0001 to 0.001 ppm for the REE and Y. The NIST 612 glass was used as an external standard and analyzed at the beginning and at the end of each line traverse and for the internal standard, the silica content of the chert was used. Furthermore, the La, Ce, Eu, Gd, and Y anomalies discussed below are calculated (Equations (1) to (5)) following the procedure of Lawrence and Kamber (2006):

$$\text{La}/\text{La}^*_{\text{MUQ}} = \text{La}_{\text{MUQ}} / (\text{Pr}_{\text{MUQ}} * (\text{Pr}_{\text{MUQ}} / \text{Nd}_{\text{MUQ}})^2) \quad (1)$$

$$\text{Ce}/\text{Ce}^*_{\text{MUQ}} = \text{Ce}_{\text{MUQ}} / (\text{Pr}_{\text{MUQ}} * (\text{Pr}_{\text{MUQ}} / \text{Nd}_{\text{MUQ}})) \quad (2)$$

$$\text{Eu}/\text{Eu}^*_{\text{MUQ}} = \text{Eu}_{\text{MUQ}} / (\text{Sm}_{\text{MUQ}}^2 * \text{Tb}_{\text{MUQ}})^{1/3} \quad (3)$$

$$\text{Gd}/\text{Gd}^*_{\text{MUQ}} = \text{Gd}_{\text{MUQ}} / (\text{Tb}_{\text{MUQ}}^2 * \text{Sm}_{\text{MUQ}})^{1/3} \quad (4)$$

$$\text{Y}/\text{Y}^*_{\text{MUQ}} = \text{Y}_{\text{MUQ}} / (0.5\text{Er}_{\text{MUQ}} * 0.5\text{Ho}_{\text{MUQ}}) \quad (5)$$

4.2. Oxygen isotopes

The oxygen isotopic compositions of selected chert samples from Meliadine (i.e., MEL-006, MEL-008 and MEL-033) were determined by Secondary Ion Mass Spectrometry (SIMS) analysis using the CAMECA 7f ion microprobe at the University of Manitoba (Winnipeg, Canada).

Prior to analysis, each polished thin section was cleaned with ethanol and polished with a 1-mircon diamond-cleaning compound to remove carbon coating that was used for the SEM analyses. They were then cleaned with soap and immersed in a dilute soap solution in an ultrasonic cleaner for 10 minutes. The protocol followed was immersion of the sections three times each for 10 minutes in the ultrasonic cleaner, successively using tap water, purified water and finally ethanol.

Fragments of John Valley Metamorphic Quartz (JValleyQtz) were used as a standard to determine instrumental mass fractionation. The standard was analysed at the beginning and at the end of each sample analysis. Looking at the acquisition method, a ≈ 2 nA primary beam of Cs^+ was accelerated at 10 kV and focused to a $15 \times 20 \mu\text{m}$ spot. An offset of 300-volts was used to eliminate molecular ion interferences. Ions were detected with a Balzers SEV 1217 electron multiplier coupled with an ion-counting system using an overall dead time of 28ns. Isotopes of ^{16}O and ^{18}O were detected by switching the magnetic field and analysis comprised 70 cycles for a total analytical time of 10 minutes. Over the four days of analyses, the external reproducibility (1σ) obtained on John Valley standard varied respectively from $\pm 0.6\text{‰}$, $\pm 0.4\text{‰}$, $\pm 0.6\text{‰}$ and $\pm 0.5\text{‰}$ (Table 5).

Ten analyses were performed on MEL-008, whereas thirty analyses were obtained for each of samples MEL-016 and MEL-033 (Table 5). In the latter two samples, the data are divided into

three different domains (e.g., B, C and D for MEL-033) to study the variability of the $\delta^{18}\text{O}$ values in different chert bands from the same thirty centimeter sample. We also note that the analyzed cherts were carefully selected to exclude any influence of accessory minerals (e.g., amphiboles, silicates, phosphate, carbonates).

Oxygen isotope compositions are reported in this study as per mil (‰) deviations (Table 5) from the Vienna Standard Mean Ocean Water (V-SMOW) using the conventional notation:

$$\delta^{18}\text{O} = [({}^{18}\text{O}/{}^{16}\text{O}_{\text{sample}}) / ({}^{18}\text{O}/{}^{16}\text{O}_{\text{V-SMOW}}) - 1] \times 1000 \text{ (6)}$$

5. Background

5.1. Rare earth element and yttrium systematics

The presence and abundance of REE+Y in chert bands may represent their primary signature, which can be influenced by one or more processes: (1) precipitation from marine water either in isolated basins or basins well connected to the open ocean (e.g., Bau and Dulski, 1996, Kamber et al., 2014); (2) precipitation from vent-sourced hydrothermal fluids (e.g., Danielson et al., 1992; Allwood et al., 2010); and (3) chemical inheritance due to replacement by silicification of precursor volcanic units (e.g., Hanor and Duchac, 1990). Chert geochemistry is also strongly dependent on the extent of contamination by terrigenous detritus (e.g., Alexander et al., 2008), volcanic ash (e.g., Klein, 2005) and oceanographic processes (e.g., phosphate and oxyhydroxide circulation and precipitation) (e.g., Alibo and Nozaki, 1999; Bau, 1999; Konhauser et al., 2005). Moreover, elements such as Sr, Ga, Sc, Zr and Th are excellent monitors of hydrogenous contamination such as detrital or volcanic input (Gourcerol et al., 2015a).

Several studies have shown that the REE+Y systematics of Archean seawater are analogous to the modern ocean with slight to moderate influence of hydrothermal vent fluids (Fig. 2; e.g., Bau and Dulski, 1996; Lawrence and Kamber, 2006; Thurston et al., 2012; Gourcerol et al., 2015a). It follows, therefore, that the shale (i.e., MUQ) normalized REE+Y pattern for the Archean seawater will be characterized by: (1) a depletion in light rare earth elements (LREE) relative to heavy rare earth elements (HREE); (2) a super-chondritic Y/Ho ratio (i.e., Y/Ho >27), yielding a positive Y/Y*_{MUQ} anomaly, commonly between 40-90; and (3) a slightly positive La anomaly (La/La*_{MUQ} between 1.15 and 1.3). These features illustrate fractionation of REE and Y in the water column resulting in preferential removal onto Mn-Fe-oxyhydroxides, organic matter, and clay particles (e.g., Kawabe et al., 1999; Bau and Koschinsky, 2009). Moreover, as the chemistry of Archean seawater was also influenced by volcanism, water-rock interaction (e.g., Veizer, 1988), and the contribution of high-temperature (>250°C) hydrothermal fluids (Fig. 2; e.g., Danielson et al., 1992; Bau and Dulski, 1999; Kamber et al., 2004; Allwood et al., 2010), these processes are characterized by variable, but well-developed positive Eu anomalies which are a product of hydrothermal processes (Fig. 2; Kamber et al., 2004). Previously, several authors also referred to a positive Gd anomaly as a seawater feature (e.g., Bau and Dulski, 1996; Lawrence and Kamber, 2006; Thurston et al., 2012) however, it has been shown that Gd is extremely sensitive to interaction of seawater with oxyhydroxides in which case it may show negative values (e.g., Alibo and Nosaki, 1999). Therefore, a positive Gd anomaly is not used in this article as an indicator of precipitation from seawater (Gourcerol et al., 2015a).

5.2. Oxygen isotopes

Cherts regardless of age are considered to have precipitated from Si-rich water initially as opal-A, then converted into opal-CT, and then finally converted to chert as a final product of dissolution-(re-)precipitation reactions during diagenesis (e.g., Knauth, 1994; Knauth and Lowe, 2003; Marin Carbonne et al., 2014) despite limited evidence of the preservation of the precursor phases (e.g., Marin-Carbonne et al., 2014; Westall et al., 2015). These aforementioned reactions involve the conversion of opal to microcrystalline chert in either in a closed (i.e., metamorphic) or open (i.e., seawater interaction) system. Marin et al. (2010) have argued for a closed system conversion based on the observed large range of $\delta^{18}\text{O}$ values (up to +14‰) for chert from the 1.8 Ga Superior-type Gunflint iron formation (Canada). These authors suggest that the amorphous silica precursor ($\delta^{18}\text{O} \approx +27‰$; from Marin et al., 2010), which precipitated at equilibrium with seawater in warm Archean ocean waters, was dissolved during diagenesis by high temperature fluids in a closed system such that the initial chert records low $\delta^{18}\text{O}$ values (e.g., ca. +14‰) but the later chert records increasingly heavier values (i.e., ca. +24 to +26‰) as a result of closed system diagenesis (i.e., a Rayleigh process). Consequently, these authors have suggested a model in which the $\delta^{18}\text{O}$ values of chert are predicted to increase continuously through the dissolution-precipitation process due to the closed nature of the system.

6. Results

6.1. Rare earth element and yttrium systematics

6.1.1. Meadowbank Area

Data for line traverse analyses on chert samples from the Central BIF, East BIF and West IF within the Meadowbank area (Gourcerol et al., 2015a) show relatively uniform REE+Y patterns (Fig. 3; table 1), with three notable exceptions (samples AMB-126232, AMB-128330

and AMB-128332 in Fig. 3A and 3C), that include a slight to moderate enrichment in HREE relative to LREE and MREE ($Nd/Yb_{MUQ} = 0.04-0.58$) that are associated with slight to moderate positive La, Y and Eu anomalies ($La/La^*_{MUQ} = 0.89-4.65$, $Y/Y^*_{MUQ} = 0.88-1.96$, $Eu/Eu^*_{MUQ} = 1.25-5.12$) and chondritic to super-chondritic Y/Ho values ($Y/Ho = 24.2-53.72$) (Table 1).

A group of samples from the East BIF (AMB-126241 and AMB-126243; Fig. 3B) and the West IF (AMB-128330, AMB-128331 and AMB-128332; Fig. 3C) show relatively flat REE patterns ($Pr/Sm_{MUQ} = 0.79 -1.03$) associated with chondritic to super-chondritic Y/Ho values ($Y/Ho = 26.02-36.71$). Enrichments in Sr (i.e., 27.9-55 ppm; and 64.9-1090 ppm), Zr (i.e., 0.97-2.17 ppm; and 19.1-43.4 ppm) and variable amounts of Th (i.e., 1.055-4.2 ppm) and Ga (i.e., 16.04-27.8 ppm) relative to the bulk of the samples is illustrated for most material from the West IF. Two samples from the Central BIF (AMB-126223 and AMB-126231; Fig. 3A) show depletion in LREE relative to the HREE, but moderate to flat patterns for the MREE and HREE that are associated with chondritic to super-chondritic Y/Ho values ($Y/Ho = 24.2-32.41$), enrichment in Zr (i.e., 104.9-183 ppm), Ga (i.e., 6.83-141.4 ppm), Sr (i.e., 20.4-95.2 ppm) and Th (i.e., 1.22-7.7 ppm) relative to other samples.

Two samples from the south of the property (i.e., AMB-128330 from West IF and AMB-126232 from Central BIF; Gourcerol et al., 2015a) show depletion in HREE relative to LREE ($Nd/Yb_{MUQ} = 2.18-7.19$) that are associated with positive La, Y and Eu anomalies (Fig. 3A,C).

Lastly, with respect to these cherts, it is noted that Ce exhibits a slight to moderate positive anomaly in the samples ($Ce/Ce^*_{MUQ} = 0.94-1.86$).

6.1.2. Meliadine Gold District

Data for chert samples from the Pump, F-Zone and Discovery deposits within the Meliadine gold district yield variable REE+Y patterns (Fig. 4; Table 2). Chert samples from the Pump deposit (Fig. 4A) are all very uniform in their chemistry and are characterized by LREE depletion ($Nd/Yb_{MUQ} = 0.06-0.75$), chondritic to sub-chondritic Y/Ho values ($Y/Ho = 11.44-32.53$), variable La and Y anomalies ($La/La^*_{MUQ} = 0.02-1.11$, $Y/Y^*_{MUQ} = 0.54-1.13$) and positive Eu anomalies ($Eu/Eu^*_{MUQ} = 2.17-6.13$) (Fig. 4A). The Y/Ho ratios for most of the samples are lower than chondritic values (i.e., 27) and correlate with negative La and Y anomalies despite a depletion in LREE which is typical of seawater input.

All chert samples from the F-Zone, except for two (MEL-015 and MEL-017), show relatively LREE-depleted patterns ($Nd/Yb_{MUQ} = 0.16-0.61$). In contrast, samples MEL015 and MEL017 show the opposite trends with slight HREE depletion ($Nd/Yb_{MUQ} = 1.19-7.21$). Overall, samples show negative to positive La anomalies associated with slight- to strong relative enrichment in Y and Eu ($La/La^*_{MUQ} = 0.42-1.43$, $Y/Y^*_{MUQ} = 1.05-1.35$, $Eu/Eu^*_{MUQ} = 2.12-8.14$) (Fig. 4B). In addition, all samples yield chondritic to super-chondritic Y/Ho values ($Y/Ho = 25.25-36.34$) and Sr enrichment (i.e., 6.5-30.6 ppm). Moderate enrichment in Zr is notable in MEL-013 and MEL-018 (i.e., 2.14-4.93 ppm).

Chert samples from the Discovery deposit show relative LREE depletion ($Nd/Yb_{MUQ} = 0.11-1.18$) except for MEL-025 ($Nd/Yb_{MUQ} = 11$; Fig. 4C). Slight to moderate enrichment for La, Y and Eu occur ($La/La^*_{MUQ} = 0.68-2.1$, $Y/Y^*_{MUQ} = 0.80-1.28$, $Eu/Eu^*_{MUQ} = 1.05-7.46$) for most samples, the exception being for MEL-038 ($La/La^*_{MUQ} = 0.47$, $Y/Y^*_{MUQ} = 0.85$, $Eu/Eu^*_{MUQ} = 2.13$) (Fig. 4C). The Y/Ho ratios vary from sub-chondritic to super-chondritic with $Y/Ho =$

18.23-37.48. In addition, most of the samples exhibit chondritic Y/Ho values associated with Sr enrichment (i.e., 0.3-177 ppm) and moderate Ga enrichment (i.e., 1.32-7.04 ppm). In contrast, samples MEL-038, MEL-039 and MEL-040 yield trace element concentrations (\pm elevated Ga). Sample MEL-038 yield low Y/Ho ratios that correlate with depletion in La and Y concentrations, which was also reported for some chert samples from the Pump deposit (Fig. 4C)

Chert samples from the Meliadine gold district show variable Ce anomalies: (1) $Ce/Ce^*_{MUQ}=0.15-1.01$ for chert samples from the Pump deposit; (2) $Ce/Ce^*_{MUQ}=0.65-1.22$ for the F-Zone deposit; and finally (3) $Ce/Ce^*_{MUQ}=0.64-2.01$ for the Discovery deposit.

6.1.3. Musselwhite Area

Data for chert samples from the chert-magnetite (4B; Fig. 5A, Table 3), the garnetiferous amphibolite (4E; Fig. 5B, Table 3), the garnet-grunerite-(chert) (4EA; Fig. 5C, Table 3), and the garnet-biotite schist (4F; Fig. 5D, Table 3) within the Musselwhite area were reported by Gourcerol et al. (2015b). It should be noted that sample E599656 from the 4B facies, samples E599660, E599665 and sample E599666 from 4EA are not illustrated in Figure 5 due to their erratic patterns that reflect some REE values approaching the limit of detection. However, these samples will be reviewed here in regard to elements lying above the detection limit.

Samples exhibit relatively uniform REE+Y patterns except for chert in the 4F facies (Fig. 5D). Most chert sampled from the 4B facies show HREE enrichment ($Nd/Yb_{MUQ} = 0.04-0.66$), yield slight to moderate positive La, Y and Eu anomalies ($La/La^*_{MUQ} = 0.8-2.35$, $Y/Y^*_{MUQ} = 0.87-1.52$, $Eu/Eu^*_{MUQ} = 2.6-3.61$) and sub-chondritic to super-chondritic Y/Ho values ($Y/Ho = 22.13-44.01$) (Fig. 5A). Sample E599656 differs from the majority of samples by its negative La and Y anomalies ($La/La^*_{MUQ} = 0.24$, $Y/Y^*_{MUQ} = 0.51$; $Eu/Eu^*_{MUQ} = 3.70$) and very low Y/Ho

value (i.e., 9.79). It is also noted that samples E599655 and E599668 are Sr enriched, (i.e., 848.8 ppm and 150.8 ppm respectively).

The two samples from the 4E show minor LREE depletion ($Nd/Yb_{MUQ} = 0.39-0.7$), are slightly to moderately La, Y and Eu enriched ($La/La^*_{MUQ} = 0.7-1.66$, $Y/Y^*_{MUQ} = 0.98-1.22$, $Eu/Eu^*_{MUQ} = 2.43-2.6$), and yield chondritic to super-chondritic Y/Ho values ($Y/Ho = 25.71-32.8$) (Fig. 5B).

The chert samples from the 4EA facies are characterized by relatively flat to slightly fractionated patterns with LREE depletion relative to HREE ($Nd/Yb_{MUQ} = 0.15-0.7$), except for samples E599654 and E599659 showing enrichment in LREE versus HREE (i.e., $Nd/Yb_{MUQ} = 2.34-2.98$). All these samples are associated with positive Eu anomalies ($Eu/Eu^*_{MUQ} = 2.34-3.97$) (Fig. 5C). Considering the La and Y anomalies along with the Y/Ho values, two groups of samples are present: (1) E599654, E599659 and E599667 show positive La and Y anomalies ($La/La^*_{MUQ} = 1.51-3.02$, $Y/Y^*_{MUQ} = 1.2-2.07$) and chondritic to super-chondritic Y/Ho ratios ($Y/Ho = 29.86-55.91$) (Fig. 5C); and (2) E599660, E599665 and E599666, which are not shown in the figure (see above), show negative La and Y anomalies ($La/La^*_{MUQ} = 0.04-0.16$, $Y/Y^*_{MUQ} = 0.22-0.73$) and very low Y/Ho ratios ($Y/Ho = 4.11-16.52$) (Fig. 5C).

The chert bands within the garnet-biotite schist (4F) facies are geochemically anomalous compared to chert from all the other studied deposits. The former samples show variable, but elevated LREE and MREE enrichments ($Pr/Sm_{MUQ} = 0.18-0.83$; $Nd/Yb_{MUQ} = 1.17-5.75$) and only moderately positive Eu anomalies ($Eu/Eu^*_{MUQ} = 1.08-1.94$) are noted (Fig. 5D). This facies is distinguished from the others by its REE+Y signature and, furthermore, is similar to the argillite studied by Thurston et al. (2012), which documented only a weak hydrothermal fluid influence.

Chert samples from the Musselwhite area exhibit variable Ce anomalies: (1) $Ce/Ce^*MUQ=0.40-1.96$ for chert samples from the 4B facies; (2) $Ce/Ce^*MUQ=0.40-1.96$ for the 4E facies; (3) $Ce/Ce^*MUQ=0.18-1.50$ for the 4EA facies; and finally (4) $Ce/Ce^*MUQ=0.74-1.25$ for the 4F facies.

6.1.4. Beardmore Geraldton Gold District

Data for chert and jasper samples from the a-type (i.e., iron oxide-rich type), b-type (i.e., siltstone-rich type) and c-type (i.e., sandstone-rich type) BIF within the Beardmore Geraldton gold district yield variable REE+Y patterns (Fig. 6, Table 4). Some samples exhibit both chert (named BG-0XX-C) and jasper (named BG-0XX-J) features, which allow a comparative study of their REE+Y systematics. However, most of the traverses are done on jasper bands as layers of pure chert are rare in this gold district.

Most of chert and jasper samples from the a-type BIF yield LREE depleted patterns ($Nd/YbMUQ=0.23-0.97$) except for the BG001-J and BG002-J samples that exhibit weak depletion in HREE relative to LREE ($Nd/YbMUQ=1.40-1.62$) (Fig. 6A). However, all chert and jasper samples show chondritic to super-chondritic Y/Ho values ($Y/Ho=28.19-38.86$), variable La and Y anomalies ($La/La^*MUQ=0.85-4.00$, $Y/Y^*MUQ=1.12-1.45$) and positive Eu anomalies ($Eu/Eu^*MUQ=1.81-4.40$) (Fig. 6A).

Chert and jasper samples from the b-type BIF show depletion in LREE relative to HREE ($Nd/YbMUQ=0.28-0.55$) except for sample BG006B-J, which exhibits the largest LREE enrichment and consequent depletion in HREE relative to LREE ($Nd/YbMUQ=1.91$) with associated slight enrichment in Th (i.e., 1.16 ppm) and Ga (i.e., 24.3 ppm) relative to other samples (Fig. 6B). However, all chert and jasper samples show chondritic to super-chondritic

Y/Ho values ($Y/Ho = 27.65-39.75$) and positive La, Y and Eu anomalies ($La/La^*_{MUQ} = 1.38-2.59$, $Y/Y^*_{MUQ} = 1.08-1.35$, $Eu/Eu^*_{MUQ} = 1.50-2.69$) (Fig. 6B).

Chert and jasper samples from the c-type BIF show relatively flat patterns and they may be divided in two distinct groups (Fig. 6C): (1) samples that exhibit depletion in LREE relative to HREE ($Nd/Yb_{MUQ} = 0.41-0.89$) that are associated with weak Sr and Sc concentrations (i.e., BG004-J, BG017-J and BG018J) relative to other samples (i.e., respectively 6.21-11.37 ppm and 3.35-4.88 ppm); and (2) samples that show depletion in the HREE relative to LREE ($Nd/Yb_{MUQ} = 1.37-2.98$) and associated with enrichment in Sr and Sc (i.e., BG004-C, BG014-J, BG016-C, BG016-J, BG019-J and BG022-J) relative to other samples (i.e., respectively 13.6-31.46 ppm and 3.0-7.2 ppm). All the samples show chondritic to super-chondritic values for Y/Ho ($Y/Ho = 24.24-37.71$), associated with positive La, Y and Eu anomalies ($La/La^*_{MUQ} = 1.11-2.14$, $Y/Y^*_{MUQ} = 0.97-1.45$, $Eu/Eu^*_{MUQ} = 1.07-3.05$) (Fig. 6C).

It is noted that chert and jasper samples from the three types of BIF exhibit slight to moderate positive Ce anomalies ($Ce/Ce^*_{MUQ} = 0.75-2.11$).

6.2. Oxygen isotopes

The $\delta^{18}O$ values for sample MEL-008 show a range from +6.6 to +19.1‰ with a mean of +14.1‰ (Fig. 7A), whereas in MEL-016, the values range from +7 to +17.3‰ and have a mean of +12.2‰ (Fig. 7B), and for sample MEL-033, values range from +11 to +16.3‰ with a mean of +14‰ (Fig. 7C). Importantly, none of the samples have values close to +27‰ which is the inferred precursor $\delta^{18}O$ value of amorphous silica predicted by Marin et al. (2010), instead, they are significantly lower by 20.4 to 7.9‰.

7. Discussion

7.1. Rare earth element and yttrium systematics

Most of the chert and jasper samples (i.e., corresponding to line traverse; Fig. 8A) from the four deposits yield similar shale-normalized systematic patterns showing depletion in LREE relative to HREE associated with positive La and Y anomalies as well as positive Eu anomalies. These observations record the influence of ambient seawater and high-temperature ($> 250^{\circ}\text{C}$) hydrothermal fluids during chert deposition.

Detrital contamination is commonly observed in several chert samples from the four deposits specifically enrichments in particular elements such as Sr, Th, Ga, Sc and Zr combined with petrographic evidences and SEM-EDS analysis. Thus, presence of apatite in a chert band (Fig. 8B) may account for elevated Sr and Th values, the presence of carbonates may account for the elevated Sr values, the presence of clay minerals may account for elevated Ga and Th values, as well zircon and monazite may account for the enrichment in Zr (Fig. 8C, D) (Gourcerol et al., 2015a). These enrichments may represent variable detrital inputs during deposition of the contained chert (Gourcerol et al., 2015a) and will significantly affect the REE+Y systematic patterns by yielding flatter patterns (compared to samples without detrital contamination), as well as chondritic values of the Y/Ho ratios (Gourcerol et al., 2015a). It is noted that no specific distinction between primary versus secondary apatite has been established in this study.

Secondary (versus primary) chemical features of few chert samples can also be pointed out by study of the REE+Y patterns as demonstrated by: (1) a depletion in HREE relative to LREE associated with positive La, Y and Eu anomalies (e.g., AMB-128330 and AMB-126232 from the Meadowbank area) due to presence of garnet (Fig. 8E) associated with the amphibolite facies

assemblages confirmed petrographically (Gourcerol et al., 2015a); as well as (2) a pronounced depletion in LREE relative to HREE suggesting presence of late carbonates (Gourcerol et al., 2015a) such as ankerite illustrated in the Musselwhite area by samples E599655 and E599668 and confirmed petrographically (Fig. 8F).

Some samples from the Meliadine district (i.e., most of samples from Pump, Mel-038 from Discovery) as well as the Musselwhite area (i.e., E599656 from the 4B, E599660, E599665 and E599666 from the 4EA) show depletion in LREE relative to HREE associated with positive Eu anomalies but differ from the bulk of samples by a lower Y/Ho ratios than chondritic values (i.e., 27) correlated with negative La and Y anomalies. Thus, this may likely reflect precipitation from high-temperature (>250°C) hydrothermal vent fluid with mixing of seawater with another influence such as Fe-oxyhydroxides.

The comparison of chert and adjacent jasper bands from the Beardmore Geraldton district does not show a notable difference from other BIF samples in this study which suggests therefore the same type of process (i.e., seawater interaction with high-T hydrothermal fluids and variable detrital contamination) during jasper deposition. In detail, jasper bands exhibit, in general, higher Fe, Ti and V and lower Si contents than chert bands which is consistent with the presence of hematite within “chert groundmass” as confirmed by petrographic study. In addition, it is noticed that on average, the associated chert bands show higher Eu anomalies than the jasper bands which suggest a greater influence of high-T hydrothermal vent fluids during its deposition.

7.2. Assessing the influence of high-temperature hydrothermal fluids

The REE+Y patterns, for all the chert samples from the Meadowbank, Meliadine, Musselwhite and Beardmore Geraldton gold districts record the influence of high-temperature

hydrothermal vent fluids (>250°C). In this section, we explore the relative importance of the hydrothermal input during chert precipitation in part by calculating binary mixing lines between a modern seawater composition from the North Pacific (Alibo and Nozaki, 1999) and a hydrothermal fluid. Shibuya et al. (2010) suggested Archean greenstone belt hydrothermal fluids were SiO₂-rich, Fe-poor, and highly alkaline in character which contrasts with the Fe-rich and acidic nature of modern hydrothermal fluids. Consequently, to more accurately constrain the Archean conditions, a 2.7 Ga brecciated chert sample (i.e., 06PCT001M; Thurston et al., 2012) characterized by an overall hydrogenous REE+Y signature associated with a strong positive Eu anomaly ($\text{Eu}/\text{Eu}^*_{\text{MUQ}} = 30.01$) that suggests a very close linkage of this chert with a hydrothermal source (Thurston et al., 2012) was chosen over modern high-T hydrothermal fluids to illustrate the hydrothermal influence in an Archean greenstone belt. Note that this high Eu/Eu* sample does not display the most likely contaminating phases based on geochemical filtering for sulfides, felsic ash and phosphates (Thurston et al., 2012). The Eu/Sm and Sm/Yb ratios are quantitative measures of the strength of the positive Eu anomaly and the flatness of the pattern that characterizes the hydrothermal fluid (Fig. 2).

According to Shibuya et al. (2010), Archean hydrothermal fluid was highly alkaline due to presence of calcite in the sea floor alteration minerals based on a high-CO₂ concentration in seawater/hydrothermal fluid. Among other factors, the hydrothermal fluid chemistry is controlled by oceanic crust composition, pH and redox conditions. The Great Oxygenation Event at ca. 2.4 Ga would have rendered seawater more oxic (e.g., van Kranendonk et al., 2012).

Most of the samples in this study fall on the mixing line despite some exhibiting high Sm/Yb ratios (Fig. 9). The Sm/Yb ratio is particularly sensitive to the presence of high-pressure residual metamorphic phases, such as amphiboles and garnets, which may overprint the primary

geochemical signature of the BIFs. For example, in the Meadowbank area (Fig. 9A), three samples are located above the mixing line (i.e., AMB-126231 from Central BIF; AMB-128330, AMB-128331 and AMB-128332 from West IF) and correspond to samples selected in the southern part of the property affected by amphibolite-facies metamorphism. In the Musselwhite area (Fig. 9C), samples from the 4F and 4EA facies also lie above the mixing line and are explained by presence of garnets. For most of the samples, the position of samples along the mixing line reflects the strength of the seawater signature.

In the Meadowbank area, samples from the Central BIF suggest an input from the high-T fluid of 1-11%, versus 3-16% for the East BIF and 0-16% for the West IF (Fig. 9A). It is noted that samples from the southern part of the West IF show a very low component of hydrothermal fluid based on their flat REE patterns. In the Meliadine gold district, most samples record a moderate hydrothermal influence (2-3% for the Discovery zone, 4-28% for the F-Zone, 3-22% for the Pump deposit) during chert precipitation (Fig. 9B). In the Musselwhite area, input from the high-T fluid was generally low during chert formation at 0-15% for the 4B facies, 4-7% for the 4E, 2-11% for the 4EA facies, and 0-5% for the 4F facies (Fig. 9C). The 4F samples seem to record more restricted influence of hydrothermal fluids, which is consistent with a slightly more positive Eu anomaly. And finally, in the Beardmore Geraldton gold district, the a-type BIF characterized by an iron oxide-rich character suggests 2-12.5% of high-T hydrothermal fluid whereas the b-type (i.e., siltstone-rich BIF) and c-type (i.e., sandstone-rich BIF) record respectively 0-5% and 0-6% (Fig. 9D).

These mixing diagrams may provide an indication of the locus of the depositional site relative to the hydrothermal source vent: when the depositional site is near the hydrothermal source vent, samples will be qualitatively closer to the high-temperature hydrothermal fluid end-

member whereas when the depositional site is more distal, the samples will be qualitatively closer to the seawater end-member. In this study, most of the studied samples have values that reflect between ≈ 0 to 20% of a high-temperature hydrothermal fluid input which may define a general lateral distance for the depositional site for Algoma-type BIF from the hydrothermal source vent. Kamber et al., (2014) have used the slope of the REE+Y plot (Pr/Yb) as a proxy for water depth but given the lack of persistent along-strike sampling, we do not attempt this sort of analysis.

7.3. Sources and influence of detrital contamination

Most chert samples from the Meadowbank, Meliadine, Musselwhite and Beardmore Geraldton areas show the influence of detrital contamination, as illustrated by flatter MUQ normalized REE patterns ($\text{Pr}/\text{Sm}_{\text{MUQ}} \approx 1$), chondritic Y/Ho ratios (i.e., $\text{Y}/\text{Ho} \approx 27$) and variations of REE+Y concentration. Despite normalization to MUQ, which is used to minimize the detrital influence in chert, some samples clearly still reflect a detrital component which indicates, therefore, that an important part of chert genesis and its study is a key to understanding the depositional setting for Algoma-type BIF. Detrital contamination may be present in chert as single mineral phases, such as phosphates, clays, and/or resistant minerals (e.g., zircon, xenotime, etc.), all of which induce a range of effects on the REE+Y patterns depending on their modal abundances (Gourcerol et al., 2015a). In order to assess the various sources of detrital contamination, a combination of ternary (La-Th-Sc) and binary element (Cr/V and Y/Ni) plots are used (Fig. 10). The La-Th-Sc ternary diagram was introduced by Bhatia and Crook (1986) to distinguish different provenances for turbidite sequences; the metabasic contamination represented by higher Sc, and felsic volcanic and clastic contamination by higher La and Th. The

Cr/V ratio reflects enrichment of Cr over other oxides, whereas Y/Ni reflects the level of ferromagnesian input compared to HREE. Ultramafic and tholeiitic sources tend to have higher Cr/V and lower Y/Ni ratios, whereas felsic- to mafic sources of calc-alkaline rocks in general have lower and higher values, respectively. In order to assess these diagrams, representative data for komatiitic and andesitic volcanic rocks are shown in the binary plots in Figure 10 for reference.

In the Meadowbank area, the La-Th-Sc plot suggests most samples represent a metabasic source for the detrital contamination (Fig. 10A). For samples AMB-128330, AMB-128331 and AMB-128332 from West IF, the flatter MUQ-normalized REE patterns suggest more felsic to mixed (i.e., felsic to mafic) sources. It should also be noted that sample AMB-126241 from East BIF is close to the mixed source domain and could also reflect bimodal contamination. Samples AMB-126223 and AMB-126231 from the Central BIF are located within or beyond the metabasic domain and could reflect metabasic clastic contamination associated with an external source and could reflect addition of volcanic ash during deposition. This hypothesis is supported by the high Zr concentration in these samples and also the positive correlation between Th and Zr in the Central BIF ($r^2 = 0.85$). The Cr/V and Y/Ni plot confirms the presence of ultramafic clastic contamination for the bulk of samples from the Meadowbank area and a mixed source for AMB-126241, AMB-128330 and AMB-128332 and felsic to intermediate calc-alkaline source for sample AMB-128331 (Fig. 10B). For AMB-126231, which is also located in the mixed source region of the plot, this confirms the presence of volcanic ash in chert bands affected by ultramafic clastic contamination and suggests that the lower content of Zr in AMB-126223 was not enough to overprint the ultramafic clastic contamination.

In the Meliadine gold district, the La-Th-Sc plot suggests a metabasic clastic contamination (Fig. 10C) for all the samples, which is confirmed by the Cr/V and Y/Ni plot (Fig. 10D).

In the Musselwhite area, the La-Th-Sc plot suggests a metabasic clastic contamination for all the samples except for one sample (E599667), which may reflect some felsic clastic contamination (Fig. 10E). It should also be noticed that a group of 4B samples differs from the majority of the other samples by their moderate La values. The Cr/V and Y/Ni plot confirms ultramafic clastic contamination for most of these samples and a felsic calc-alkaline clastic source for E599667 (Fig. 10F). However, for samples E599655 and E599668 from unit 4B, which exhibit moderate La enrichment in the La-Th-Sc plot, they show high Y/Ni ratios which could suggest contamination by a mafic calc-alkaline source, such as basalt or gabbro, rather than ultramafic contamination for these two samples.

In the Beardmore Geraldton gold district, the La-Th-Sc plot suggests a metabasic contamination for most of the samples (Fig. 10G), with some exceptions: (1) sample BG004-C from the c-type BIF, which may reflect either granitic gneiss contamination or a mixed source of detrital contamination in the chert band. This observation is consistent with the enrichment in Th and Zr observed in this sample (cf. REE+Y systematics section); and (2) sample BG006B-J from the b-type BIF shows higher La and Th concentrations than other samples from this BIF and may reflect either a mixed source of detrital contamination which is consistent with Th and Ga enrichments in this sample or a metabasic source with high La (cf. REE+Y systematics study). However, these observations are not illustrated in the Cr/V and Y/Ni plot (Fig. 10H) which confirms a mixed source of detrital contamination for BG004-C, in which the felsic influence is much lower than the mafic contamination, and probably a metabasic source for BG006B-J with its high La, Th and Ga values.

In general, a component of ultramafic clastic contamination is illustrated for the four deposits and is consistent with the Keewatin Stratigraphy (e.g., Lawson, 1885; Thurston and Chivers, 1990) for Algoma-type BIF deposition and therefore the most important clastic contamination is likely komatiite and tholeiitic material. Moreover, local volcanic ash and some felsic to intermediate calc-alkaline clastic material in addition to felsic to mafic calc-alkaline clastic contamination are suggested for the Meadowbank and Musselwhite samples, respectively.

7.3.1. Assessing the detrital contamination input

To estimate the degree of influence of the detrital component within BIFs, a conservative mixing line was calculated using seawater samples selected in the North Pacific from Alibo and Nozaki (1999) and the MUQ composite as end-members and using the $(Pr/Nd)_{MUQ}$ ratios as a measure of the flatness of the pattern and chondritic values of Y/Ho ratio characteristic of detrital contamination (Fig. 11). The MUQ end member represents a perfect example of the influence of detrital contamination within an Archean greenstone belt as the mud represents a basaltic provenance with minor felsic volcanic input. Before discussing these plots, it is noted that the bulk of the samples lie just below the calculated mixing line, which represents the high-temperature hydrothermal input to the samples. In the following discussion, the percentage values should be considered to represent the relative influence of the end members rather than quantitative measures.

In the Meadowbank area, samples from the Central BIF suggest $\approx 8-100\%$, the East BIF $\approx 50-100\%$ and the West IF $\approx 30-100\%$ detrital influence during chert precipitation suggesting that East BIF and West IF are the BIFs most affected by detrital contamination in the Meadowbank area (Fig. 11A). The East BIF shows more hydrothermal influence than the Central BIF and

West IF samples, which is consistent with where samples plotted in Figure 9A. All these samples are located either on the mixing line or below it, which suggests the influence of a detrital component, a seawater influence and also a high-temperature hydrothermal fluid input during precipitation of the chert bands.

In the Meliadine gold district, some samples differ from those from Meadowbank by their lower Y/Ho ratios, which are mainly observed in the Pump samples and MEL-025 and MEL-038 from Discovery (Fig. 11B). Considering only samples located on or directly below the mixing line, Discovery samples suggests 60-100%, F-Zone samples 65-100% and Pump samples \approx 85-95% detrital influence during chert precipitation. All the samples from the F-Zone and most from Discovery (except MEL-025 and MEL-038) are located either on or below the mixing line which suggests the significant influence of a detrital component, seawater influence and high-temperature hydrothermal fluid input during precipitation of chert bands.

In the Musselwhite area, as in the Meliadine gold district, some samples differ by their low Y/Ho ratios mainly observed in the 4B, 4EA and 4F facies. Considering only samples located on or directly below the mixing line, the detrital influence during chert precipitations is estimated at 40-100% for 4B, 80-100% for 4E, and 0-85% for 4EA (Fig. 11C). Based on these observations, the 4EA seems to be “relatively less affected” by detrital contamination than the other facies and 4B the most influence of hydrothermal fluids.

In the Beardmore Geraldton gold district, samples from the a-type BIF suggest 60-90% detrital contamination, samples from the b-type BIF indicate 58-100% and finally samples from the c-type BIF suggest 65-100% detrital influence during chert and jasper precipitation (Fig. 11D). The a-type BIF appears the least affected by detrital contamination and is consistent with

the nature of b- and c-type BIF which are intercalated, respectively, with siltstone and sandstone layers.

The percentage of detrital contamination discussed above is indicative of the general degree of contamination allowing a comparison of the different chert samples as most of the samples showing $\approx 100\%$ MUQ contamination on the mixing trends also show a seawater signature based on their positive La and Y anomalies and REE fractionation patterns. Thus, this treatment confirms that a small amount of clastic detritus in the chert bands is sufficient to dominate the bulk REE signature of the cherts as proposed by Gourcerol et al. (2015a). We also note that we have previously documented the effects of small amounts of detrital apatite, xenotime, zircon, and garnet on REE+Y plots (Gourcerol et al., 2015a).

Focusing on samples from the Meliadine gold district and Musselwhite area that show low Y/Ho ratios (Figs. 11B, C), it is suggested that another factor and/or environmental control may be involved which is not considered in the mixing model above. In this case, we note that the fractionation between Y and Ho during particle scavenging by Fe-oxyhydroxides (rather than Mn-oxyhydroxides in an Archean context) may explain the Y/Ho ratios lower than chondritic values based on the experimental observations of Bau (1999). In this latter work it was shown that scavenging of REE+Y can occur in a restricted environment and Fe-oxyhydroxide REE+Y patterns can display less positive or even negative La and Y anomalies associated with a M-type lanthanide tetrad effect (Masuda et al., 1987). These observations are consistent with the good correlation noted in this study between the low Y/Ho and negative La and Y anomalies observed in the chert samples. Therefore, it is suggested the REE and trace element chemistry of the studied chert samples may illustrate the influence of coeval precipitation of Fe-oxyhydroxides in a restricted basin isolated from recharge from an open ocean. In such a case, the isolation of such

a basin from open ocean influence is reflected in the chert chemistry that inherits a chemical signature which in part is due to scavenging of REE+Y by contemporaneous Fe-oxyhydroxides (e.g., Kawabe et al., 1999; Bau, 1999; Minami et al., 1998).

7.4. Mechanical versus biological processes controlling chert precipitation

As previously suggested, some of the Meliadine and Musselwhite samples may reflect a primary signature derived by scavenging by Fe-oxyhydroxide particulate matter in a restricted basin isolated from seawater influence (i.e., low Y/Ho ratio associated with negative La and Y anomalies; Bau, 1999). The precipitation of Fe-oxyhydroxides in Archean seawater can be explained both by mechanical and biological processes considering that seawater was devoid of free oxygen (e.g., Konhauser et al., 2005; Shibuya et al., 2010; Fig. 12). In the mechanical-process model of Shibuya et al. (2010), a dynamic pH modification during the mixing of alkaline, SiO₂-rich and Fe-poor hydrothermal fluids with acidic to neutral, silica-saturated, Fe-rich Archean seawater causes precipitation of Fe³⁺ from Fe²⁺-rich seawater as well as silica under anoxic conditions (Figs. 12A, 13). This process is illustrated by reaction 7:



In contrast to the former model, the biological-process model (Fig. 12B) of Konhauser et al. (2005) refers to biological oxidation of Fe²⁺ which occurs in ocean bottom waters near the seafloor by photoautotrophic bacteria. This model can be divided into two stages (i.e., photoautotrophic activity and sedimentation), described below.

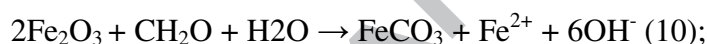
Initially, photoautotrophic Fe²⁺ is oxidized by bacteria, which results in formation of Fe-hydroxide (reaction 8; Posth et al., 2013):



Sedimentation of these Fe-hydroxides (e.g., ferrihydrite) occurs at the bottom of the water column and during formation of the oxide bands, the Fe:C ratio changes and produces an excess of Fe(III) in the sediments, which leads to preferential mobilization of fermentation products relative to Fe(III) and results in precipitation of hematite (reaction 9; Posth et al., 2013):



Moreover, if a biomass is present in the environment, the hematite is transformed to siderite or magnetite through the reactions below (10) and (11):



In order to explore the potential role played by the presence of Fe-oxyhydroxides on chert geochemistry, mixing lines were calculated based on the Alibo and Nozaki (1999) seawater composition, Fe-oxyhydroxide precipitates, and graphitic mudstone from the Meliadine gold district (i.e., the KMG unit) as end members using the $\text{La}/\text{La}^*_{\text{MUQ}}$ and $\text{Y}/\text{Y}^*_{\text{MUQ}}$ ratios as their polarity reflects respectively seawater-dominated or Fe-oxyhydroxide-dominated precipitation. The results are summarized in Figure 14. In detail, Fe-oxyhydroxide precipitates produced under experimental conditions in both a restricted environment from acidic seawater (Bau, 1999) and from alkaline solutions (Kawabe et al., 1999) are used for comparison. The KMG samples are graphitic mudstones and may represent a carbon reservoir that reflects biological oxidation of Fe^{2+} and which shows low Y/Ho ratios associated with negative La and Y anomalies, hence having a chemistry consistent with formation in a restricted basin (Table 6).

The distribution of samples from the Meadowbank area (Fig. 14A) illustrate the domination of a primary seawater signature despite the fact that interaction with Fe-oxyhydroxides is highlighted by positive variations of La and Y anomalies along the mixing lines. Within an open seawater system, it is difficult to attribute formation of Fe-oxyhydroxides to either pH variation or biological oxidation in an environment devoid of oxygen. Nonetheless, pH variation is strongly suggested as a result of seawater and hydrothermal mixing (i.e., acidic versus alkaline; Figs. 9A, 13A). In contrast, the biological influence, as illustrated by the presence of a carbonaceous argillite (i.e., the KMG samples), appears to have generated weak Y enrichment. Therefore, samples from Central BIF and East BIF suggest a combination of pH variation and biological processes, whereas the West IF suggests mainly pH variation for Fe-oxyhydroxide precipitation.

In the Meliadine gold district, the bulk of samples are also located in the seawater domain of Figure 14B (blue dashed box) except for samples showing negative La and Y anomalies (i.e., from Pump and MEL-025 and MEL-028), for which Fe-oxyhydroxide dominates the primary signature. In detail, three trends are observed: (1) interaction along or slightly below the mixing line with samples from Bau (1999), which reflects acidic pH with variable biological influence (i.e., mainly F-Zone); (2) interaction along a mixing line with samples from Kawabe et al., (1999) which reflect slightly-neutral to alkaline pH (i.e., Discovery); and (3) interaction along the mixing line with KMG samples in the purple dashed box (Fig. 14B). Thus, two mechanisms for precipitation of Fe-oxyhydroxide are proposed for these samples: (1) influence of dynamic pH between alkaline hydrothermal fluids and acidic-neutral seawater; and (2) biological oxidation of Fe^{2+} . Moreover, samples associated with group (3) suggest deposition in a restricted basin under a biological influence.

In the Musselwhite area, three groups are illustrated in Figure 14C: (1) a group of samples reflecting interaction of seawater with Fe-oxyhydroxides (i.e., positive La and Y anomalies); (2) a group of samples illustrating domination of Fe-oxyhydroxides on the primary signature (i.e., E599656 from 4B; E599660, E599665 and E599666 from 4EA) and which are closely associated with the KMG-seawater mixing line; and (3) a group of samples showing weak negative La and Y anomalies associated with low Y/Ho ratios and which are similar to Fe-oxyhydroxide samples from Bau (1999) (i.e., E599670 and E599671 from 4B; E599657 and E599658 from 4F and E599652 from 4E). The first group of samples reflects interaction of seawater with Fe-oxyhydroxide and domination of the primary signature by seawater as previously seen for Meadowbank and Meliadine and may reflect variable pH conditions. The second group of samples reflects domination of Fe-oxyhydroxide on the primary signature associated with biological oxidation. Finally, the third group of samples may represent domination of the primary signature by Fe-oxyhydroxides precipitated under conditions similar to those described by Bau (1999) and involving acidic pH.

Samples from the Beardmore Geraldton gold district, in which hematitic inclusions in jasper bands are presumed to reflect Fe-oxyhydroxide precipitation in chert bands, show interaction of seawater with Fe-oxyhydroxides (Fig. 14D) and domination of the seawater influence on the primary signature of chert and jasper. Most of these samples show correlation with the Fe-oxyhydroxides from Bau (1999), which were obtained experimentally from acidic seawater. It is noted that three samples from the a- and b-type BIF fall below the mixing line of seawater with KMG which may reflect interaction of seawater with Fe-oxyhydroxide precipitated under biological influence.

7.4.1. pH condition relationships

In modern hydrothermal systems, pH and redox conditions of high temperature hydrothermal fluids are strongly buffered by the mineral assemblage of plagioclase + epidote + anhydrite. This process maintains the value of pH around 5 (as confirmed by *in situ* pH measurements of deep-sea high temperature hydrothermal fluid; e.g., Ding et al., 2005). In the Archean, it appears that calcite (rather than anhydrite) and igneous plagioclase precipitated due to extremely low sulfate concentration in the seawater (Kump and Seyfried, 2005) suggesting that CO₂ concentration in the Archean hydrothermal fluid was high enough to precipitate calcite compared to modern basalt-hosted hydrothermal fluids which have CO₂ up to 0.02 mol/kg.

By calculation, Shibuya et al. (2010) demonstrated that, in this mineral-buffered system, the minimum pH *in situ* depends on CO₂, and the CO₂ of a hydrothermal fluid in the early Archean is considered to be at least 0.2 mol/kg. This condition gives highly alkaline pH *in situ* (>10) because the presence of calcite keeps Ca²⁺ very low in the hydrothermal fluid as opposed to the modern equivalent.

In parallel to what has been already discussed, several related studies have suggested that given the anoxic character of Archean seawater, the shale-normalized REE+Y patterns for Archean seawater differ from the modern seawater based on the behavior of Ce which shows a well-developed, negative Ce anomaly in the latter due to oxidation of Ce⁺³ to Ce⁺⁴ in the stratified water column resulting in preferential removal onto Mn-Fe-oxyhydroxides, organic matter, and clay particles (e.g., Kawabe et al., 1999; Bau and Koschinsky, 2009; Planavsky et al., 2010). However, Bau (1999) experimented with the scavenging of dissolved REE+Y by precipitating Fe-oxyhydroxide in a restricted environment at pH values ranging from 3.6 to 6.2

and ambient oxygen content (i.e., oxic conditions) and demonstrated that pH has a more important effect on Ce than oxygen in presence of Fe-oxyhydroxides. Thus, at a $\text{pH} \leq 5$ oxidative scavenging of Ce is favored in the presence of Fe-oxyhydroxide and generates a positive Ce anomaly (Fig. 15) and in $\text{pH} \geq 5$, REE+Y systematics shows a negative Ce anomaly associated with an M-type lanthanide tetrad effect (Fig. 15). Therefore, we only consider Ce anomalies to be significant with respect to oxygenation status when open basin conditions prevail.

Based on the above, samples for Pump, MEL-025, MEL-028 and the second group of samples from Musselwhite (previously described in this section) reflect deposition in a restricted environment, and show negative Ce anomalies that may reflect precipitation at a $\text{pH} > 5$. As the KMG samples also show negative Ce anomalies ($\text{Ce}/\text{Ce}^*_{\text{MUQ}} = 0.14-0.47$), this suggests their formation at $\text{pH} > 5$ and, therefore, that samples from Pump, MEL-025, MEL-028 and the second group of sample from Musselwhite may reflect domination of the primary signature by Fe-oxyhydroxides formed by biological processes. It is noted, however, that in an open system the Ce anomaly has to be used with some caution as biological processes appears to drive the binary mixing lines of pH variation to the right on Fig. 14 which suggests Y enrichment.

7.5. Influence of post-depositional events on primary isotopic and trace element signatures of the chert

It is now recognized that post-depositional processes (i.e., diagenesis, metamorphism, hydrothermal fluids) have negligible influence on the REE+Y composition in BIF (e.g., Bau, 1993; Bau and Dostal, 1996; Bolhar et al., 2004; Webb et al., 2009; Thurston et al., 2012), which is further supported by the results of this study. However, in contrast to this stability, the results of recent microanalysis of the oxygen isotopic signature of chert from BIF using *in situ* SIMS

measurements (e.g., Marin et al., 2010; Marin-Carbonne et al., 2011, 2012, 2013, 2014; Robert and Chaussidon, 2012) have demonstrated that post-depositional perturbation of the primary $\delta^{18}\text{O}$ signal is variably developed in samples. In order to further evaluate such modification, we have also undertaken similar *in situ* SIMS $\delta^{18}\text{O}$ analysis of certain of our chert samples used for the trace element work to track such modification and assess its relevance to the present study.

For the purpose of also assessing the influence of post-depositional processes on cherts, the $\delta^{18}\text{O}$ values were determined on three selected chert samples from the Meliadine area. The results of the oxygen isotopic study suggest: (1) modification of the $\delta^{18}\text{O}$ values caused by oxygen isotopic fractionation due to dissolution of precursor amorphous silica during diagenesis; and (2) an open system until sealing of the chert-system occurred which avoids an increase of the $\delta^{18}\text{O}$ chert through the combined effects of dissolution-precipitation and isotopic fractionation (as discussed earlier in this section).

The fractionation of oxygen isotopes is temperature-sensitive and thus it may be used as a means to assess the temperature of the fluids mediating the reaction process whereby opal is converted to chert. Thus, in order to address the potential influence of post-depositional fluids and to define the intensive parameters associated with the replacement process, we have undertaken modeling using the equations of Taylor (1998). For this, we have assumed the primary amorphous silica had a $\delta^{18}\text{O} = +27\text{‰}$ (Marin et al., 2010) and that it reacted to form chert with final $\delta^{18}\text{O}$ values between +6.6 to +19.1‰ by interacting with fluids. For the latter, we use four different reacting fluids (i.e., $\delta^{18}\text{O}_{\text{H}_2\text{O}} = 0, 5, 10$ and 15‰) to represent seawater through to metamorphic fluid values at variable temperature (30° to 400°C; Hoefs, 2009). These results are summarized in Figure 16 and form the basis of the following discussion.

For a fluid with $\delta^{18}\text{O}_{\text{H}_2\text{O}} = 0\text{‰}$ (i.e., ocean water), the modelling suggests high-temperature (>100°C) interaction of fluid with amorphous silica is required to obtain the observed chert $\delta^{18}\text{O}$ values (i.e., +6.6 to +19.1‰). It is accepted that the Archean oceanic temperature was around 70°C (e.g., Knauth and Lowe, 1978, 2003), but higher values are not realistic. Thus, for the parameters discussed above, it is unlikely that Archean seawater interacting with original opal could produce the observed $\delta^{18}\text{O}$ values in the chert samples (Fig. 16A).

For a fluid with $\delta^{18}\text{O}_{\text{H}_2\text{O}}$ values of +5 and +10‰, the modelling suggests that temperatures >200°C and >250°C, respectively (Figs. 16B, C) are required to account for the observed $\delta^{18}\text{O}$ chert values of between +11 to +19‰, which represent 80% of the dataset. These temperatures would equate to the onset of metamorphic conditions (i.e., zeolite facies) and require deep burial.

Finally, for a fluid with $\delta^{18}\text{O}_{\text{H}_2\text{O}} = +15\text{‰}$, the parameters used in the modelling do not provide any plausible scenarios to explain the observed $\delta^{18}\text{O}_{\text{chert}}$ values (Fig. 16D). The higher temperature (i.e., $\geq 300^\circ\text{C}$) and isotopic parameters ($\delta^{18}\text{O}_{\text{H}_2\text{O}} = +15\text{‰}$) equate to a typical metamorphic fluid, as documented for regional metamorphism or orogenic gold mineralization (e.g., Taylor, 1974; Goldfarb et al., 2005), which has been implicated by Marin et al. (2010) where chert has the appropriate $\delta^{18}\text{O}$ values.

In summary, although the lower $\delta^{18}\text{O}$ values recorded by cherts (i.e., from +6.6 to +11‰) may be interpreted as evidence for a hot Archean seawater, it is unlikely that such fluids could penetrate the crust and be heated to the necessary temperatures (i.e., 100° to 400°C) and not exchange with the host rocks and thus have their $\delta^{18}\text{O}$ signature modified to higher values. For these reasons, such a singular fluid model is not considered a viable explanation for the observed ranges in the $\delta^{18}\text{O}_{\text{chert}}$. At the other extreme, a singular model using $\delta^{18}\text{O}_{\text{H}_2\text{O}} = +15\text{‰}$ would

require very high temperatures. A compromise is therefore found for a fluid of $\delta^{18}\text{O}_{\text{H}_2\text{O}} = +5\text{‰}$ which may represent fluid present during diagenesis, essentially an isotopically modified downwelling and heated sea water sourced fluid with an original $\delta^{18}\text{O}_{\text{H}_2\text{O}} = 0\text{‰}$. In this model, the $\delta^{18}\text{O}_{\text{chert}}$ records both a change in the reacting fluid as it interacts with the crust and also as it heats up. This fluid:chert interaction would proceed until the system was essentially sealed. This hypothesis is also supported by the fact that REEs and trace element concentrations in chert bands do not show resetting of their primary signature (as seen previously in this paper) suggesting that a fluid with very low concentration of REEs and trace elements was responsible for conversion of opal to chert. The chemical data for the ambient seawater, which show a range of REE concentration normalized to MUQ between 10^{-7} to 10^{-8} (Fig. 2), would therefore satisfy this requirement and is why the $\delta^{18}\text{O}$ values for chert change whereas their REE +Y systematic do not.

8. Conclusions

Chert bands sampled from BIF horizons in four gold deposit settings in Canada (Meadowbank, Meliadine, Musselwhite and Beardmore Geraldton) were used to validate the restricted basin model for BIF proposed by Barrett et al. (1988a) in which seawater is not considered to have been of uniform chemistry. The use of *in situ* LA ICP-MS analyses obtained via a traverse mode on carefully selected chert bands within the BIF using appropriate analytical protocols provide quantitatively meaningful data at low detection limits (i.e., to 0.0001 to 0.001 shale-normalized values). The consistency of the patterns noted in this study indicates, importantly, that primary chemical signatures have been retained within the selected chert material despite several post-formation deformation and metamorphic events, in some cases to

amphibolite facies. In contrast to the trace element chemistry, *in situ* analysis of $\delta^{18}\text{O}$ indicates the cherts record extensive oxygen isotopic exchange during conversion of primary opal to microcrystalline silica. Based on detailed REE+Y geochemistry and petrographic studies, the chert bands are interpreted to reflect the following:

1. Most samples from the four deposits record the influence of seawater during precipitation, as illustrated by depletion in the LREE relative to the MREE and HREE with associated positive La and Y anomalies. These chemical features suggest deposition in either a partially closed basin under the constant influence of seawater or within an open seawater system.
2. The influence of high-temperature (>250°C) hydrothermal vent fluid during deposition is reflected by a positive Eu anomaly. Importantly, it is suggested here that this anomaly may provide indirect information about proximity to the vent and thus important information about the deposition site for BIF; thus, the stronger the Eu anomaly, the closer to the vent site. The influence of a detrital input is illustrated from petrographic and SEM-EDS imaging by the presence of apatite, xenotime and zircon grains that occur disseminated in chert bands, in addition to the enrichment in the REE, elevated chondritic Y/Ho values and variably elevated values for Th, Ga, Zr, Sc and Sr. Furthermore, an evaluation of chemical contamination from ultramafic (i.e., komatiite or tholeiite) and minor volcanic ash and felsic to intermediate calc-alkaline clastic material is consistent with the stratigraphic proportions in a Keewatin sequence model for Algoma-type BIF deposition (e.g., Thurston et al., 2008).
3. Domination of the primary signature by particle scavenging by Fe-oxyhydroxide phases, as revealed by negative La, Gd and Y anomalies in some samples from the Meliadine and

Musselwhite areas, suggest BIF deposit occurred in a restricted basin environment, involving no REE+Y recharge from the open ocean to re-equilibrate the REE+Y budget. The Fe-oxyhydroxides, rather than Mn-oxyhydroxides, are favoured due to the presumably anoxic deep Archean seawater setting, as Mn-oxyhydroxides precipitate in the presence of oxygen and dissolve through the anoxic water column; the latter is common in modern oceans which are more oxic than their Archean precursors (e.g., Kawabe et al., 1999; Bau and Koschinsky, 2009).

4. The negative Ce anomalies in some of the chert samples indicates precipitation of Fe-oxyhydroxide occurred at a pH > 5, most of the cherts from the four deposits studied have positive Ce anomalies and may reflect precipitation at a pH < 5. This conclusion suggests that Archean high-temperature hydrothermal vent fluids from which oxyhydroxides originate may represent an alkaline hydrothermal fluid, as proposed by Shibuya et al. (2010).
5. Lastly, an *in situ* detailed study of $\delta^{18}\text{O}$ for three chert samples from the Meliadine gold district suggests the influence of a fluid $\delta^{18}\text{O}_{\text{H}_2\text{O}} = 0$ to 5‰ at high-temperature (>100°C) during diagenesis within an open system, as illustrated by modification of the precursor amorphous silica $\delta^{18}\text{O}$ value caused by oxygen isotopic fractionation due to dissolution-precipitation processes. However, it is noted that contrary to the $\delta^{18}\text{O}$ values, the REEs and trace elements are not modified as the reacting fluid, of sea water origin, is characterized by very low-REE concentrations.

6. Acknowledgements

The authors gratefully acknowledge the staff of Agnico Eagle Mines Ltd., Goldcorp Ltd. and Premier Gold. The authors also thank Dr. Matthew Leybourne, Dr. Sally Pehrsson, Dr. Olivier Côté-Mantha, and John Biczok for discussions regarding the geochemistry and regional geological setting of the study areas. The LA-ICP-MS analyses were done in the Geochemical Fingerprinting Laboratory at Laurentian University with the assistance of Dr. J. Petrus and the oxygen isotope analyses were performed at the University of Manitoba (Winnipeg) with the capable assistance of R. Sharp. Finally, we sincerely acknowledge the contribution of Dr. Benoit Dubé, Dr. Sebastien Castonguay and Dr. Patrick Mercier-Langevin of the Geological Survey of Canada for their input and continued support. The study is supported by both TGI-4 funding from Natural Resources Canada and funding through a Natural Sciences and Engineering Research Council Collaborative Research and Development agreement with participation by Agnico Eagle Mines Ltd and Goldcorp Ltd. We thank also Drs. L. Brengman and an anonymous reviewer for their constrictive comments that helped to substantially improve the manuscript.

7. References

- Alexander, B.W., Bau, M., Andersson, P. and Dulski, P., 2008. Continentally-derived solutes in shallow Archean sea water; rare earth element and Nd isotope evidence in iron formation from the 2.9 Ga Pongola Supergroup, South Africa; *Geochimica et Cosmochimica Acta*, v. 72, p. 378-394.
- Alibo, D. S. and Nozaki, Y., 1999. Rare earth elements in seawater: particle association, shale-normalization, and Ce oxidation; *Geochimica et Cosmochimica Acta*, v. 63, p. 363–372.

Allwood, A.C., Kamber, B.S., Walter, M.R., Burch, I.W. and Kanik, I., 2010. Trace element record depositional history of an Early Archean stromatolitic carbonate platform; *Chemical Geology*, v. 270, p. 148-163.

Armitage, A.E., James, R.S. and Goff, S.P., 1996. Gold mineralization in Archean banded iron formation, Third Portage Lake area, Northwest Territories, Canada; *Exploration and Mining Geology*, v. 5, no. 1, p. 1-15.

Aspler, L.B., and Chiarenzelli, J.R. 1996a. Stratigraphy, sedimentology and physical volcanology of the Henik Group, central Ennadai-Rankin greenstone belt, Northwest Territories, Canada: Late Archean paleogeography of the Hearne Province and tectonic implications; *Precambrian Research*, v. 77, p. 59-89.

Barnes, S.J, Heggie, G.J and Fiorentini, M.L., 2013. Spatial variation in platinum group element concentrations in ore-bearing komatiite at the Long-Victor deposit, Kambalda Dome, Western Australia: enlarging the footprint of nickel sulfide orebodies; *Economic Geology*, v. 108, p. 913-933

Barrett, T.J., Fralick, P.W., and Jarvis, I., 1988a. Rare-earth-element geochemistry of some Archean iron formations north of Lake Superior, Ontario; *Canadian Journal of Earth Sciences*, v. 25, p. 570–580.

Bau, M. 1993. Effects of syn- and post-depositional processes on the rare-earth element distribution in Precambrian iron-formations; *European Journal of Mineralogy*, v. 5, p. 257-267.

Bau, M. and Dulski, P., 1996. Distribution of Y and rare-earth elements in the Penge and Kuruman Iron Formations, Transvaal Supergroup, South Africa; *Precambrian Research*, v. 79, p. 37-55.

Bau, M. and Dulski, P., 1999. Comparing yttrium and rare earths in hydrothermal fluids from the Mid-Atlantic Ridge: implications for Y and REE behavior during near-vent mixing and for the Y/Ho ratio of the Proterozoic seawater; *Chemical Geology*, v. 155, p. 70-90.

Bau, M., 1999. Scavenging of dissolved yttrium and rare-earths by precipitating iron oxyhydroxide: Experimental evidence for Ce oxidation, Y-Ho fractionation, and lanthanide tetrad effect; *Geochimica et Cosmochimica Acta*, v. 63, no. 1, p.67-77.

Bau, M. and Koschinsky, A., 2008. Oxidative scavenging of cerium on hydrous Fe oxide: Evidence from distribution of rare earth elements and yttrium between Fe oxides and Mn oxides in hydrogenetic ferro manganese crusts; *Geochemical Journal*, v. 43, p. 37- 47.

Bekker, A., Slack, J.F., Planavsky, N., Kraepz, B., Hofmann, A., Konhauser, K.O. and Rouxel, J., 2010. Iron formation: the sedimentary product of a complex interplay among mantle, tectonic, oceanic and biospheric processes; *Economic Geology*, v. 105, p. 467-508.

Bhatia, M.R. and Crook, K.A.W., 1986. Trace elements characteristics of graywackes and tectonic setting discrimination of sedimentary basins; *Contributions to Mineralogy and Petrology*, v. 92, p. 181-193.

Biczok, J., Hollings, P., Klipfel, P., Heaman, L., Maas, R., Hamilton, M., Kamo, S. and Friedman, R., 2012. Geochronology of the North Caribou greenstone belt, Superior Province Canada: Implications for tectonic history and gold mineralization at the Musselwhite mine; *Precambrian Research*, v. 192-195, p. 209-230.

Bolhar, R., Van Kranendonk, M.J. and Kamber, B.S., 2005. A trace element study of siderite-jasper banded iron formation in the 3.45 Ga Warrawoona Group, Pilbara craton-Formation from hydrothermal fluids and shallow seawater; *Precambrian Research*, v. 137, p. 93-114.

Breaks, F.W., Osmani, I.A. and DeKemp, E.A., 2001. Geology of the North Caribou Lake area, northwestern Ontario; Ontario Geological Survey, Open File Report 6023, 80 p.

Carpenter, R.L., 2004. Relative and absolute timing of supracrustal deposition, tectonothermal activity and gold mineralization, West Meliadine region, Rankin Inlet greenstone belt, Nunavut, Canada; PhD. Thesis, Faculty of Graduate Studies, University of Western Ontario, 362 p.

Carpenter, R.L., Duke, N.A., Sandeman, H.A., Stern, R., 2005. Relative and absolute timing of gold mineralization along the Meliadine Trend, Nunavut, Canada; evidence for Paleoproterozoic

gold hosted in an Archean greenstone belt.; *Economic Geology and the Bulletin of the Society of Economic Geologists*, v. 100, p. 567-576.

Danielson, A., Moeller, P. and Dulski, P., 1992. The europium anomalies in banded iron formations and the thermal history of the oceanic crust; *Chemical Geology*, v. 97, p. 89-100.

Davis, W.J., Ryan, J.J., Sandeman, H.A., and Tella, S., 2008. A Paleoproterozoic detrital zircon age for a key conglomeratic horizon within the Rankin Inlet area, Kivalliq region, Nunavut: implications for Archean and Proterozoic evolution of the area; *In Current research 2008-8*, Geological Survey of Canada, 10 p.

DeBaar, H.J.W, Bacon, M.P and Brewer, P.G., 1985. Rare earth elements in the Pacific and Atlantic Oceans; *Geochemica et Cosmochimica Acta*, v. 49, p. 1943-1959.

Ding, K., Seyfried Jr., W.E., Zhang, Z., Tivey, M.K., Von Damm, K.L., and Bradley, A.M., 2005. The in situ pH of hydrothermal fluids at mid-ocean ridge; *Earth and Planetary Science Letters*, v. 237, p. 167-174.

Fralick, P. and Pufahl, P.K., 2006. Iron formation in Neoproterozoic deltaic successions and the microbially mediated deposition of transgressive systems tracts; *Journal of Sedimentary Research*, v. 76, p. 1057-1066.

Goodwin, A.M., 1973. Archean iron-formations and tectonic basins of the Canadian Shield; *Economic Geology*, v. 68, p. 915-933.

Gourcerol, B., Thurston, P.C., Kontak, D.J., Côté-Mantha, O., 2015a. Interpretations and implications of preliminary LA ICP-MS analysis of chert for the origin of geochemical signatures in banded iron formations (BIFs) from the Meadowbank gold deposit, Western Churchill Province, Nunavut; *Chemical Geology*, v. 410, p. 89-107.

Gourcerol, B., Thurston, P.C., Kontak, D.J., Côté-Mantha, O., and Biczok, J. 2015b. The geochemistry of chert from the Banded Iron Formation-type Musselwhite and Meadowbank gold deposits: Distinguishing primary and mineralization-related signatures of chert: *Geological Survey of Canada, Current Research 2015-1*, 24 p.

Gross, G.A., 1980. A classification of iron-formations based on depositional environments; *Canadian Mineralogist*, v. 100, p.1511-1527.

Hall, R.S. and Rigg, D.M., 1986. Geology of the West Anticline Zone, Musselwhite Prospect, Opapimiskan Lake, Ontario, Canada, *In: Macdonald, A.J. (Ed.), Gold '86; an international symposium on the geology of gold deposits; proceedings volume; GOLD '86*, Toronto, ON, Canada, p. 124-136.

Hanor, J.S. and Duchac, K.C., 1990. Isovolumetric silicification of early Archean komatiites; geochemical mass balances and constraints on origin; *Journal of Geology*, v. 98, p. 863-877.

Hoefs, J., 2009. Stable isotope geochemistry; 6th Edition Springer Berlin, Heidelberg, 293p.

Holland, H.D., 2003. The geologic history of seawater; *In* Treatise on Geochemistry

Edited by H.D. Holland and K.K. Turekian. Pergamon, Oxford, p. 583-625.

Hollings, P., and Kerrich, R., 1999 Trace element systematics of ultramafic and mafic volcanic rocks from the 3 Ga North Caribou greenstone belt, northwestern Superior Province.

Precambrian Research, v. 93, p. 257–279.

Hrabi, R.B., Barclay, W.A., Fleming, D. and Alexander, R.B., 2003. Structural evolution of the

Woodburn Lake group in the area of the Meadowbank gold deposit, Nunavut; *In* Current

Research 2003-C27, Geological Survey of Canada, 10 p.

James, H.L., 1954. Sedimentary facies iron-formation; *Economic Geology*, v. 49, p. 235-293.

Janvier, V., Castonguay, S., Mercier-Langevin, P., Dubé, B., McNicoll, V., Pehrsson, S., Malo,

M., De Chavigny, B. and Cote-Mantha, O., 2015a. Preliminary results of geology of the Portage deposit, Meadowbank gold mine, Churchill Province, Nunavut, Canada; Geological Survey of

Canada, Current Research 2015-2, 18 p. doi:10.4095/295532

Kamber, B.S., Bolhar, R. and Webb, G.E., 2004. Geochemistry of late Archean stromatolites from Zimbabwe: evidence for microbial life in restricted epicontinental seas; *Precambrian Research*, v. 132, p. 379-399.

Kamber, B.S., Greig, A. and Collerson, K.D., 2005. A new estimate for the composition of weathered young upper continental crust from alluvial sediments, Queensland, Australia; *Geochimica et Cosmochimica Acta*, v. 69, p. 1041–1058.

Kamber, B.S. and Webb, G.E., 2007. Transition metal abundances in microbial carbonate: a pilot study based on in situ LA-ICP-MS analysis; *Geobiology*, v. 5, p. 375-389.

Kamber, B.S., Webb, G.E. and Gallagher, M., 2014. The rare earth element signal in Archaean microbial carbonate: information on ocean redox and biogenicity; *Journal of the Geological Society, London* v. 171, p. 745-763.

Kappler, A., Pasquero, C., Konhauser, K.O. and Newman D.K., 2005. Deposition of banded iron formations by anoxygenic phototrophic Fe(II)-oxidizing bacteria; *Geology*, v. 33, p. 865-868.

Kawabe, I., Ohta, A., Ishii, S., Tokumura, M. and Miyauchi, K., 1999b. REE partitioning between Fe–Mn oxyhydroxide precipitates and weakly acid NaCl solutions: Convex tetrad effect and fractionation of Y and Sc from heavy lanthanides; *Geochemical Journal*, v. 33, p. 167–179.

Kawabe, I., 1978. Calculation of oxygen isotope fractionation in quartz-water system with special reference to the low temperature fractionation. *Geochimica et Cosmochimica Acta*, v.42, p. 613-621.

Kita, I., Taguchi, S. and Matsubaya, O., 1985. Oxygen isotope fractionation between amorphous silica and water at 34-93°C. *Nature*, v. 314, p. 83-84.

Klein, C., 2005. Some Precambrian banded iron-formation (BIFs) from around the world: Their age, geologic settings, mineralogy, metamorphism, geochemistry, and origin; *American Mineralogist*, v. 90, p. 1473-1499.

Knauth L. P. and Lowe D. R., 1978. Oxygen isotope geochemistry of cherts from Onverwacht Group (3.4 billion years), Transvaal, South-Africa, with implications for secular variations in isotopic composition of cherts; *Earth Planetary Science Letter*, v. 41, p. 209-222.

Knauth, L.P., 1994. Petrogenesis of chert, *In*: Heaney, P.J.P., Prewitt, C.T., Gibbs, G.V. (Eds.), *Silica: Physical Behavior, Geochemistry and Materials Applications*; Mineralogical Society of America, p. 233–258.

Knauth, L.P. and Lowe, D.R., 2003. High Archean climatic temperature inferred from oxygen isotope geochemistry of chert in the 3.5 Ga Swaziland Supergroup; *Geological Society of America Bulletin*, v. 115, p. 566–580.

Konhauser, O.K., Newman, D.K. and Kappler, A., 2005. The potential significance of microbial Fe(III) reduction during deposition of Precambrian banded iron formations; *Geobiology*, v. 3, p. 167-177.

Kresz, D.U. and Zayachivsky, B., 1991. Precambrian Geology, northern Long Lac area; Ontario Geological Survey, Report 273.

Kump, L.R., Seyfried Jr., W.E., 2005. Hydrothermal Fe fluxes during the Precambrian: effect of low oceanic sulfate concentrations and low hydrostatic pressure on the composition of black smokers; *Earth and Planetary Science Letters*, v. 235, p. 654–662.

Lafrance, B., DeWolfe, J.C. and Stott, G M., 2004. A structural reappraisal of the Beardmore-Geraldton Belt at the southern boundary of the Wabigoon subprovince, Ontario, and implications for gold mineralization; *Canadian Journal Earth Sciences*, v. 41, p. 217-235.

Lawley, C.J.M., Dubé, B., Mercier- Langevin, P., Kjarsgaard, B., Knight R. and Vaillancourt, D., 2015. Defining and mapping hydrothermal footprints at the BIF-hosted Meliadine gold district, Nunavut, Canada; *Journal of Geochemical Exploration*, v.155, p. 33-55.

Lawrence, M. G. and Kamber, B. S., 2006. The behavior of the rare earth elements during estuarine mixing- revisited; *Marine Chemistry*, v. 100, p. 147-161.

Lawson, A.C., 1885. Report on the geology of the Lake of the Woods region, with special reference to the Keewatin (Huronian?) belt of the Archean rocks; Geological Survey of Canada, Annual Report (new series), v.I, Report CC, 151 p.

Lécuyer, C. and Allemand, P., 1999. Modelling of the oxygen isotopes evolution of seawater: implications for the climate interpretation of the $\delta^{18}\text{O}$ of marine sediments; *Geochimica et Cosmochimica Acta*, v. 63, p. 351–361.

Longerich, H. P., Jackson, S. E. and Gunther, D., 1996. Laser ablation inductively coupled plasma mass spectrometric transient signal data acquisition and analyte concentration calculation; *Journal of Analytical Atomic Spectrometry*, v. 11, p. 899-904.

Mackasey, W.O., Edwards, G.R., and Cape, D.F., 1976. Legault Township, District of Thunder Bay; Ontario Division of Mines, Preliminary Map P-1191, scale 1: 15 840.

Marin, J., Chaussidon, M. and Robert, F., 2010. Microscale oxygen isotope variations in 1.9 Ga Gunflint cherts: assessments of diagenesis effects and implications for oceanic paleo-temperature reconstructions; *Geochimica et Cosmochimica Acta*, v. 74, p. 116-130

Marin-Carbonne, J., Chaussidon, M., and Robert, F., 2010. Micrometer-scale chemical and isotopic criteria (O and Si) on the origin and history of Precambrian cherts: Implications for paleotemperature reconstructions; *Geochimica et Cosmochimica Acta*, v. 92, p. 129-147.

- Marin-Carbonne, J., Chaussidon, M., Boiron, M.C. and Robert, F., 2011. A combined in situ oxygen, silicon isotopic and fluid inclusion study of a chert sample from Onverwacht Group (3.35 Ga, South Africa): new constraints on fluid circulation; *Chemical Geology*, v. 286, p. 59-71.
- Marin-Carbonne, J., Chaussidon, M. and Robert, F., 2012. Micrometer-scale chemical and isotopic criteria (O and Si) on the origin and history of Precambrian cherts: implications for paleo-temperature reconstructions; *Geochemica et Cosmochimica Acta*, v. 92, p. 129-147.
- Marin-Carbonne, J., Faure, F., Chaussidon, M., Jacob, D. and Robert, F., 2013. A petrographic and isotopic criterion of the state of preservation of Precambrian cherts based on the characterization of the quartz veins; *Precambrian Research*, v. 231, p. 290-300.
- Marin-Carbonne, J., Robert, F. and Chaussidon, M., 2014. The silicon and oxygen isotope compositions of Precambrian cherts: A record of oceanic paleo-temperatures? ; *Precambrian Research*, v. 247, p. 223-234.
- Masuda, A. and Ikeuchi, Y., 1979. Lanthanide tetrad effect observed in marine environment; *Geochemical Journal*, v. 13, p. 19-22.
- Masuda, A., Kawakami, O., Dohmoto, Y. and Takenaka, T., 1987. Lanthanide tetrad effects in nature: two mutually opposite types, W and M; *Geochemical Journal*, v. 21, p. 119-124.

Matsuhisa, Y., Goldsmith, J.R., and Clayton, R.N., 1979. Oxygen isotopic fractionation in the system quartz-albite-anorthite-water. *Geochimica et Cosmochimica Acta*, v. 43, p. 1131-1140.

McLennan, S.M., Hemming, S., McDaniel, D.K. and Hanson, G.N., 1993. Geochemical approaches to sedimentation, provenance and tectonics; Geological Society of America, Special Papers 1993, v. 284, p. 21-40.

McNicoll, V., Dubé, B., Biczok, J., Castonguay, S., Oswald, W., Mercier-Langevin, P., Skulski, T., and Malo, M., 2013. The Musselwhite gold deposit, North Caribou greenstone belt, Ontario: new high-precision U-Pb ages and their impact on the geological and structural setting of the deposit; Abstract, Geol. Assoc. of Canada annual meeting, Winnipeg.

Minami, M., Masuda, A., Takahashi, K., Adachi, M. and Shimizu, H., 1998. Y-Ho fractionation and lanthanide tetrad effect observed in cherts; *Geochemical Journal*, v. 32, p. 405-419.

Moran, P., 2008. Litho-geochemistry of the sedimentary stratigraphy and metasomatic alteration in the Musselwhite gold deposit. North Caribou Lake metavolcanic-metasedimentary belt, Superior Province, Canada: implications for deposition and mineralization; Unpublished Master's Thesis, Lakehead University, 351 p.

Ohmoto, H., Watanabe, Y., Yamaguchi, K.E., Naraoka, H., Haruna, M., Kakegawa, T., Hayashi, K., and Kato, Y., 2006. Chemical and biological evolution of early Earth: Constraints from banded iron formations; Geological Society of America Memoire, v. 198, p. 291-331.

Oswald, W., Castonguay, S., Dubé, B., McNicoll, V.J., Biczok, J., Malo, M. and Mercier-Langevin, P., 2015. Geological setting of the world-class Musselwhite gold Mine, Superior Province, northwestern Ontario, and implications for exploration, In: Targeted Geoscience Initiative 4: Contributions to the Understanding of Precambrian Lode Gold Deposits and Implications for Exploration, (ed.) B. Dubé and P. Mercier-Langevin; Geological Survey of Canada, Open File 7852, p. 69–84

Otto, A., 2002. Ore forming processes in the BIF-hosted gold deposit Musselwhite Mine, Ontario, Canada. Unpublished Master's Thesis, Freiberg Institute of Mining and Technology, 86 p.

Pehrsson, S.J., Wilkinson, L. and Zaleski, E., 2004. Geology of the Meadowbank gold deposit area, Nunavut; Geological Survey of Canada, Open File 4269, scale 1:20 000.

Pehrsson, S.J., Berman, R.G., Davis, W.J., 2013. Paleoproterozoic orogenesis during Nuna aggregation: a case study of reworking of the Rae craton, Woodburn Lake, Nunavut; *Precambrian Research*, v. 232, p. 167-188.

Planavsky, N., Bekker, A., Rouxel, O.J., Kamber, B.S., Hofmann, A.W., Knudsen, A. and Lyons, T.W., 2010. Rare Earth Element and yttrium compositions of Archean and Paleoproterozoic Fe formations revisited: New perspectives on the significance and mechanisms of deposition; *Geochimica et Cosmochimica Acta*, v. 74, p. 6387-6405.

Posth, N.R., Kohler, I., Swanner, E.D., Schroder, C., Wellmann, E., Binder, B., Konhauser, K.O., Neumann, U., Berthold, C., Nowak, M. and Kappler, A., 2013. Simulating Precambrian banded iron formation diagenesis; *Chemical Geology*, v. 362, p. 66-73.

Pufahl, P.K., Pirajno, F. and Hiatt, E.E., 2013. Riverine mixing and fluvial iron formation: A new type of Precambrian biochemical sediment; *Geology*, v. 41, n. 12, p. 1235-1238.

Robert, F. and Chaussidon, M., 2006. A palaeo-temperature curve for the Precambrian oceans based on silicon isotopes in cherts; *Nature*, v. 443, p. 969-972.

Shanks, W.S., 1993. *Geology of Eva and Summer Townships, District of Thunder Bay; Ontario Geological Survey, Open File Report 5821.*

Sherlock, R., Pehrsson, S., Logan, A.V., Hrabí, R.B. and Davis, W.J., 2004. Geologic setting of the Meadowbank gold deposits, Woodburn Lake group, Nunavut; *Exploration Mining Geology*, v. 13 (1-4), p. 67-107.

Sherlock, R.L., Alexander, R.B., March, R. and Barclay, W.A., 2001a. Geologic setting of the Meadowbank iron formation-hosted gold deposits; *In Current Research 2001-C11, Geological Survey of Canada*, 23 p.

Sherlock, R.L., Alexander, R.B., March, R. and Barclay, W.A., 2001b. Geologic setting of the Meadowbank iron formation-hosted gold deposits; Geological Survey of Canada, Open File 3149, scale 1:10 000.

Shibuya, T., Komiya, T., Nakamura, K., Takai, K. and Maruyama, S., 2010. Highly alkaline, high-temperature hydrothermal fluids in the early Archean ocean; *Precambrian Research*, v. 182, p. 230-238.

Taylor, H.P., 1974. The application of oxygen and hydrogen isotope studies to problems of hydrothermal alteration and ore deposition; *Economic Geology*, v. 69, p. 843-883.

Taylor, H.P., 1978. Oxygen and hydrogen isotope studies of plutonic granitic rocks; *Earth Planetary Science Letter*, v. 38, p. 177-210.

Tella, S., Paul, D., Berman, R.G., Davis, W.J., Peterson, T.D., Pehrsson, S.J., and Kerswill, J.A., 2007. Bedrock geology compilation and regional synthesis of parts of Hearne and Rae domains, western Churchill Province, Nunavut-Manitoba; Geological Survey of Canada, Open File 5441, scale 1:550 000 (3 sheets and a CD-ROM).

Tóth, Z., Lafrance, B., Dube, B., McNicoll, V.J., Mercier-Langevin, P., and Creaser, R.A., 2015. Banded iron formation-hosted gold mineralization in the Geraldton area, northwestern Ontario: Structural setting, mineralogical characteristics, and geochronology, In: *Targeted Geoscience Initiative 4: Contributions to the Understanding of Precambrian Lode Gold Deposits and*

Implications for Exploration, (ed.) B. Dube and P. Mercier-Langevin; Geological Survey of Canada, Open File 7852, p. 85–97.

Thurston, P.C. and Chivers, K.M., 1990. Secular variation in greenstone sequence development emphasizing Superior Province, Canada; *Precambrian Research*, v.46, p.21-58.

Thurston, P.C., Ayer, J.A., Goutier, J. and Hamilton, M.A., 2008. Depositional gaps in Abitibi greenstone belt stratigraphy: a key to exploration for syngenetic mineralization; *Economic geology*, v. 103, p. 1097-1134.

Thurston, P.C., Kamber, B.S. and Whitehouse, M., 2012. Archean cherts in banded iron formation: Insight into Neoproterozoic ocean chemistry and depositional processes; *Precambrian Research*, v. 214-215, p. 227-257.

Tomlinson, K.Y., Hall, R.P., Hughes, D.J., and Thurston, P.C., 1996. Geochemistry and assemblage accretion of metavolcanic rocks in the Beardmore–Geraldton greenstone belt, Superior Province; *Canadian Journal of Earth Sciences*, v. 33, p. 1520-1533.

Van Kranendonk, M.J., Altermann, W., Beard, B.L., Hoffman, P.F., Johnson, C.J., Kasting, J.F., Melezhik, V.A., Nutman, A.P., Papineau, D., and Pirajno, F. 2012. A chronostratigraphic division of the Precambrian ; possibilities and challenges; In Gradstein, F.M, Ogg, J.G., Schmitz, M.D., Ogg, G.J. (Eds.), *The Geologic Time Scale 2012*; Elsevier, Boston, USA, pp. 299–39

Vearncombe, S. and Kerrich, R., 1999. Geochemistry and Geodynamic setting of volcanic and plutonic rocks associated with early Archean volcanogenic massive sulphide mineralization, Pilbara Craton; *Precambrian Research*, v. 98, p. 243-270.

Veizer, J., 1988. The evolving exogenic cycle; *In Chemical cycles in the evolution of the Earth Edited by B.C. Gregor, R.M. Garrels, F.T. Mackenzie and B.J. Maynard*. Wiley-Interscience, New York, p. 175-218.

Westall, F., Campbell, K.A., Br  h  ret, J.G., Foucher, F., Gautret, P., Hubert, A., Sorieul, S., Grassineau, N. and Guido, D.M., 2015. Archean (3.33 Ga) microbe-sediment systems were diverse and flourished in a hydrothermal context; *Geology*, v. 43, p. 615-618.

Webb, G.E., Nothdurft, L.D., Kamber, B.S., Kloprogge, J.T. and Zhao, J.X., 2009. Rare earth element geochemistry of scleractinian coral skeleton during meteoric diagenesis: A sequence through neomorphism of aragonite to calcite; *Sedimentology*, v. 56, p. 1433-1463.

Wright, G.M., 1967. Geology of the southeastern barren grounds, Parts of the Districts of Mackenzie and Keewatin. Geological Survey of Canada, Memoire 350, 91 p.

Figure Caption

Figure 1. Field and laboratory photographs of BIF to show the nature of sampling used in the study: (A) Outcrop of BIF in the Meadowbank gold area. The inset is a close up to illustrate the nature of the chert and magnetite layering; (B) Polished thin section of chert (Qtz) and magnetite (Mt) layers made from the previous sample. The black solid line represents the line traverse done during LA ICP-MS study; and (C) Back-scattered electron image from the SEM illustrating the line traverse (upper right corner) done in the chert (Qtz) band.

Figure 2. MUQ - normalized REE+Y patterns illustrating the chemical signatures of the two modern settings relevant to this study, namely, modern seawater composition (from the North Pacific; Alibo and Nozaki, 1999) and a hydrothermal vent fluid developed over basaltic and ultramafic substrate (Bau and Dulski, 1999).

Figure 3. MUQ - normalized REE+Y patterns for BIF-hosted cherts from samples in different parts of the Meadowbank area: (A) Central BIF, (B) East BIF, and (C) West IF.

Figure 4. MUQ - normalized REE+Y patterns for BIF-hosted cherts from samples in different parts of the Meliadine gold district: (A) Pump, (B) F-Zone, and (C) Discovery.

Figure 5. MUQ - normalized REE+Y patterns for BIF-hosted chert from samples in different parts of the Musselwhite area: (A) 4B - Oxide dominant facies excluding sample E599656, (B) 4E – garnetiferous amphibolite samples, (C) 4EA - garnet-grunerite samples excluding samples E599660, E599665 and E599666, and (D) 4F – biotite-garnet schist samples.

Figure 6. MUQ- normalized REE+Y patterns for BIF-hosted chert from samples in different parts of the Beardmore Geraldton gold district: (A) a-type – iron oxide-rich type, (B) b-type – siltstone-rich type, and (C) c-type - sandstone-rich type. Note that the lettering refers to chert (C) and jasper (J) types of silica layers.

Figure 7. Variation in the $\delta^{18}\text{O}$ values versus analysis number for chert samples from Meliadine gold district: MEL-008 (A), MEL-016 (B) and MEL-033 (C).

Figure 8. Back-scattered electron image from the SEM for different BIF-hosted chert samples from the Meadowbank and Musselwhite: (A) an example of line traverse done in a chert band (Qtz) during LA ICP-MS analysis (from E599668); (B) example of mineral inclusions in a chert band which includes anhedral apatite (Ap), euhedral pyrite (Py) and variable subhedral to anhedral amphibole (Amp) (from AMB-126247); (C) subhedral chlorite (Chl) and amphibole (Amp) grains surrounding subhedral to euhedral zircon (Zrn) grains in chert band (from AMB-126231); (D) subhedral to euhedral grains of chlorite (Chl) with an inclusion of euhedral zircon (Zrn) in chert band (from AMB-126223); (E) traverse line in centre of the image done in a chert band at the edge of a garnet (Gr) band (from AMB-126232); and (F) ankerite (Ank) surrounding subhedral apatite (Ap) grains in a chert band (from E599655).

Figure 9. Binary plots of elemental ratio data (Eu/Sm and Sm/Yb) for chert samples in BIFs from Meadowbank (A), Meliadine (B), Musselwhite (C), and Beardmore Geraldton (D). These plots are used to assess the potential influence of high-T hydrothermal fluids on the chert chemistry, as illustrated with the conservative mixing line. The data for the high-T hydrothermal fluid is from Thurston et al., (2012) and data for seawater is from Alibo and Nozaki (1999).

Figure 10. Trace element plots (La-Th-Sc and Cr/V and Y/Ni; respectively modified from Bhatia and Crook, 1986; and modified from McLennan et al., 1993) used to constrain the provenance of detrital contamination in chert bands from the BIF localities: (A) and (B) from the Meadowbank area, (C) and (D) from Meliadine gold district, (E) and (F) from the Musselwhite area, and (G) and (H) from the Beardmore Geraldton gold district.

Figure 11. Binary plots of Y/Ho versus and $(Pr/Sm)_{MUQ}$ for chert samples from the Meadowbank area (A), the Meliadine gold district (B), the Musselwhite area (C) and the Beardmore Geraldton gold district (D) BIFs. These plots are used to assess the potential influence of detrital contamination in the chert layers, as illustrated with the conservative mixing line. The data for the MUQ and seawater are from Kamber et al. (2005) and Alibo and Nozaki (1999), respectively. The dashed arrow represents the influence of a high-T hydrothermal fluid and the grey square presented in Meliadine and Musselwhite represents the influence of Fe-oxyhydroxides.

Figure 12. Model of Algoma-type BIF deposition on Archean seafloor: (A) the mechanical-process model illustrated by progressive decrease of pH from the silica-chimney through the seawater column; (B) the biological-process model illustrated by oxidation of photoautotrophic produced Fe(II) follow by sedimentation of Fe-hydroxide leading to fermentation and release of Fe(III). Several meters away from the vents, the emissions become white and turbid by precipitation of the oversaturated silica; while with increasing distance from the vent, a cloud of reddish brown particles of iron oxyhydroxides dominates hydrothermal plumes. In the vicinity of the hydrothermal vent systems, the silica particles are predominant in the hydrothermal sediments, but the iron oxyhydroxides are abundant with increasing distance from the vent systems (modified from Konhauser et al., 2005 and Shibuya et al., 2010).

Figure 13. Redox path for precipitation of Fe-oxyhydroxide by mixing of acidic to neutral seawater and alkaline hydrothermal fluids in a low temperature seawater setting. The black arrow represents the mixing of acidic seawater with Fe^{2+} in solution with alkaline hydrothermal fluids that leads to precipitation of $Fe(OH)_3$ (modified from Pufahl et al., 2013).

Figure 14. Binary plots of Y/Y^* and La/La^* that illustrate the effect of Fe-oxyhydroxide precipitation on the primary seawater signature of cherts from the Meadowbank area (A), the Meliadine gold district (B), the Musselwhite area (C), and the Beardmore Geraldton gold district (D). The blue dashed box represents the open seawater environment, whereas the purple dashed box a restricted basin where the primary signature is dominated by particle scavenging. The data for the Fe-oxyhydroxides are from Bau (1999) and illustrate Fe- oxyhydroxide

precipitates from experimental condition in acidic pH (purple rhombs) whereas the data from Kawabe et al. (1999) reflect experimental results from solutions with neutral to alkaline pH with a variable influence of NaCl solution (purple triangles). KMG samples (turquoise rhombs) from Meliadine illustrate microbial Fe^{3+} reduction. Black arrow represents the increase of pH whereas dashed black arrow refers to the biological influence. Note that sample E599664 from 4F in Musselwhite is omitted due to its low REE values which, preclude calculating the Y/Y^* parameter. It is notable in this context that sample 06PCT001M (from Thurston et al., 2012), selected to illustrate the hydrothermal influence in an Archean greenstone belt (cf. hydrothermal assessment), reflects interaction of Fe-oxyhydroxide from alkaline pH solution with seawater which is consistent with the Shibuya et al., (2010) model and, therefore, promotes the use of this sample as a proxy for the influence of Archean hydrothermal fluids.

Figure 15. Plot of MUQ - normalized REE+Y patterns for experimentally produced Fe-oxyhydroxide precipitates at variable pH values (data from Bau, 1999). The black arrow indicates the increasing pH values.

Figure 16. Diagram summarizing the variation of calculated values of $\delta^{18}\text{O}_{\text{chert}}$, using the equations of Taylor (1978) and variety of appropriate silica- H_2O ^{18}O fractionation factors (Kawabe, 1978; Matsuhisa et al., 1979; Kita et al., 1985), as a function of temperature (30° to 300°C) and water/rock ratios for four reacting fluids having $\delta^{18}\text{O}_{\text{H}_2\text{O}} = 0, +5, +10$ and $+15\%$ (respectively A, B, C, and D). The shaded area represents the range of $\delta^{18}\text{O}$ values (i.e., $+6.6$ to $+19.1\%$) obtained for chert from the Meliadine gold district. Note that the value of the initial $\delta^{18}\text{O}_{\text{chert}}$ was assumed to be $+27\%$, which is the value of precursor amorphous silica in Archean BIF settings (Marin et al., 2010).

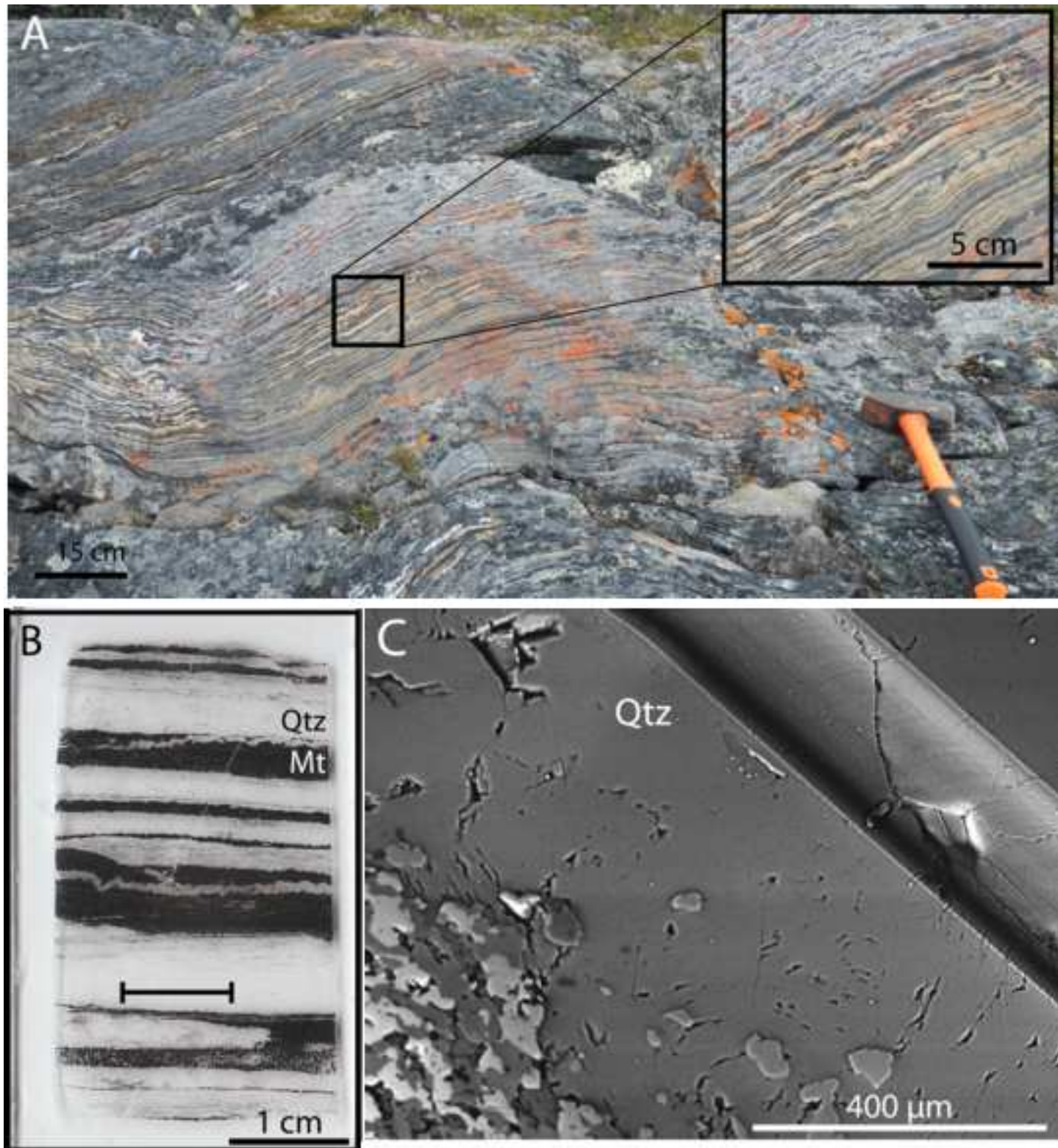
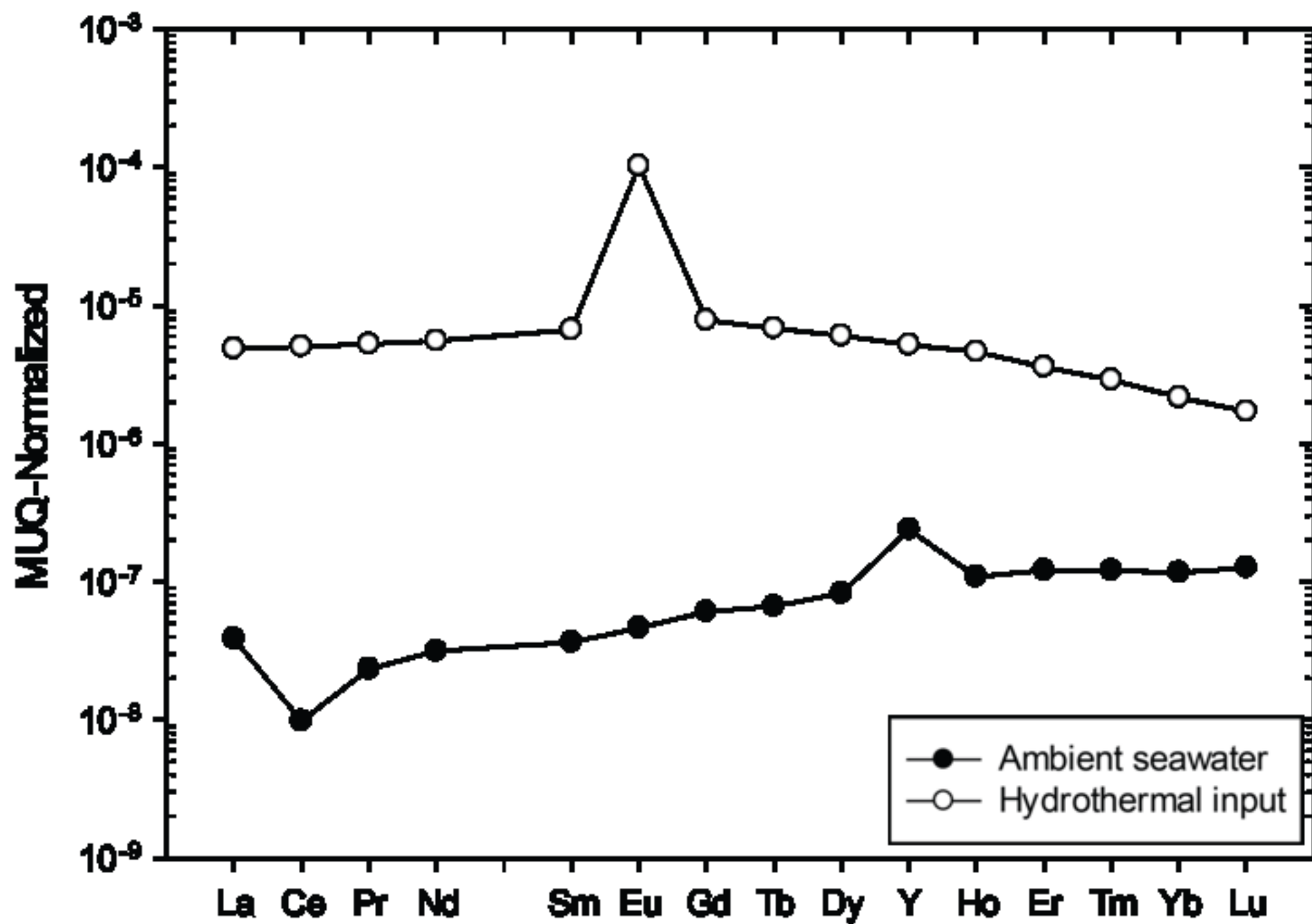
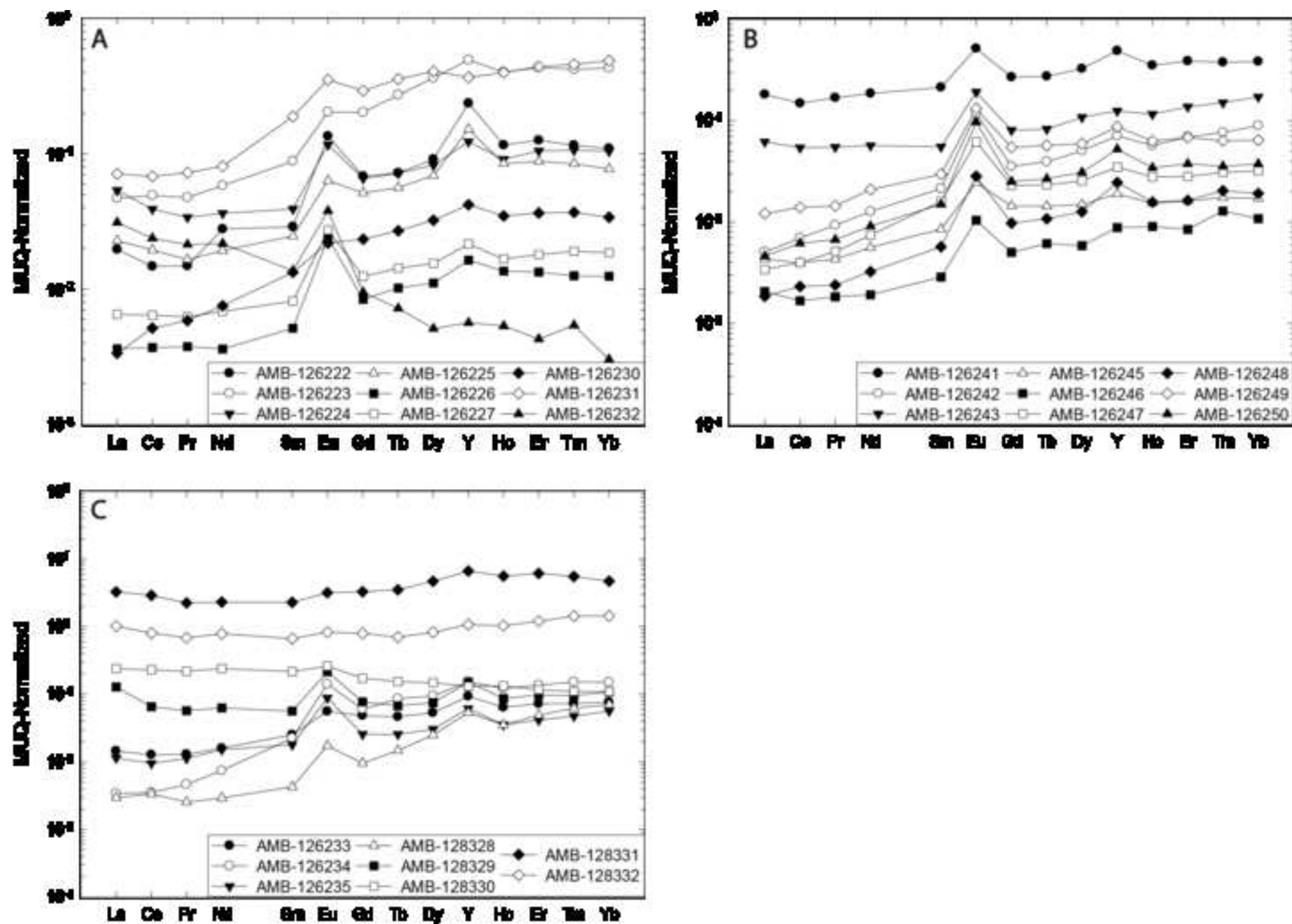
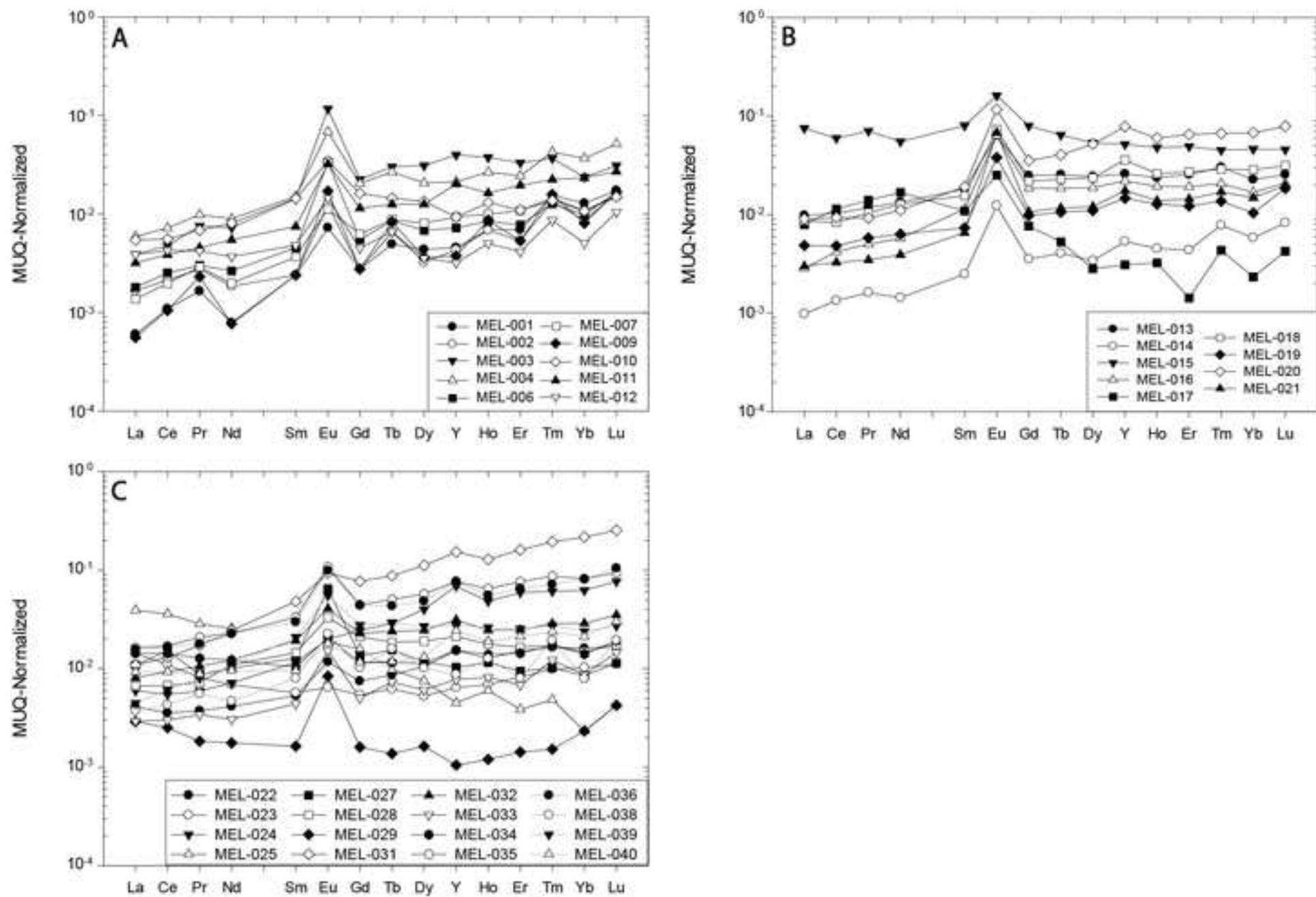


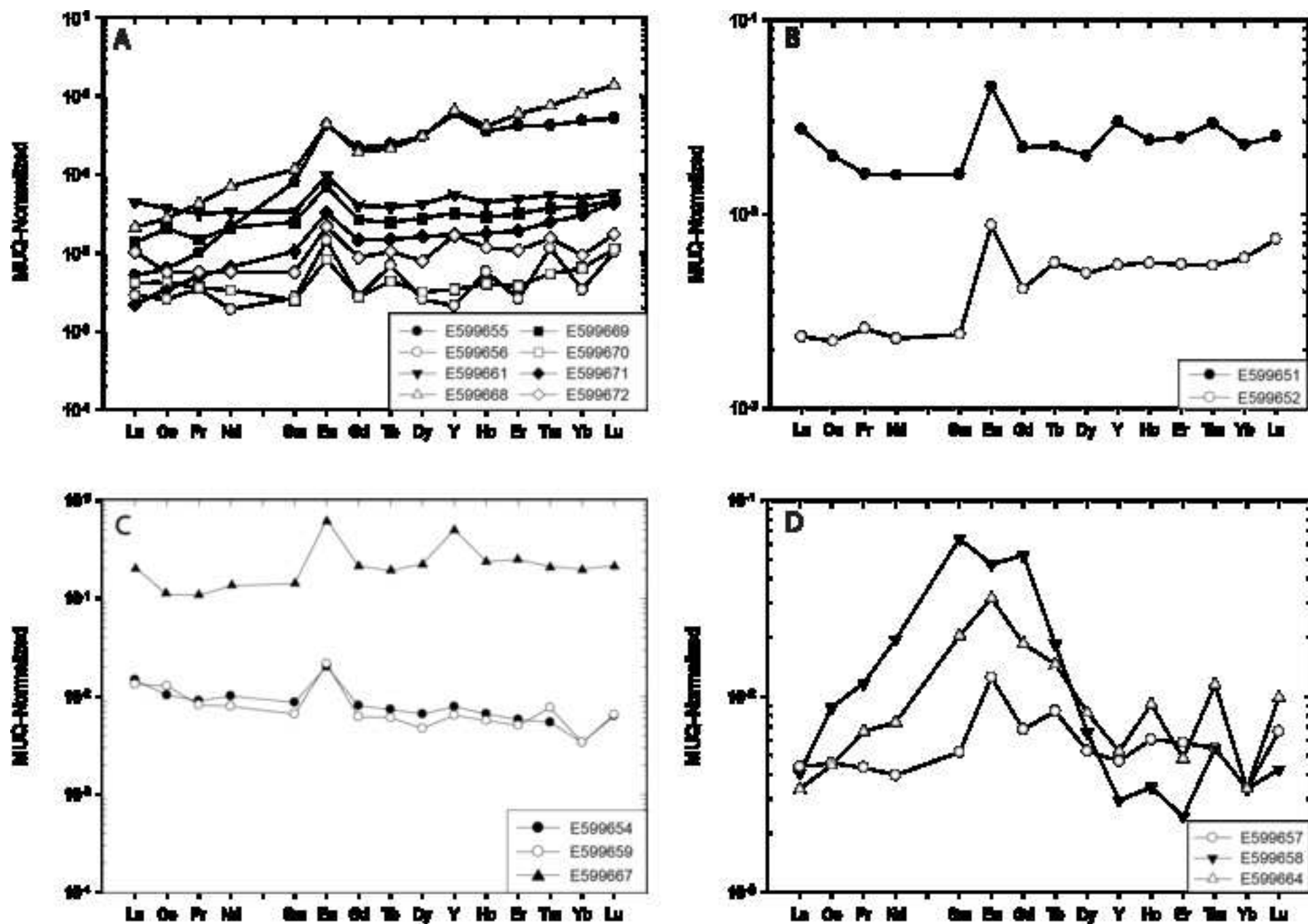
Figure 2

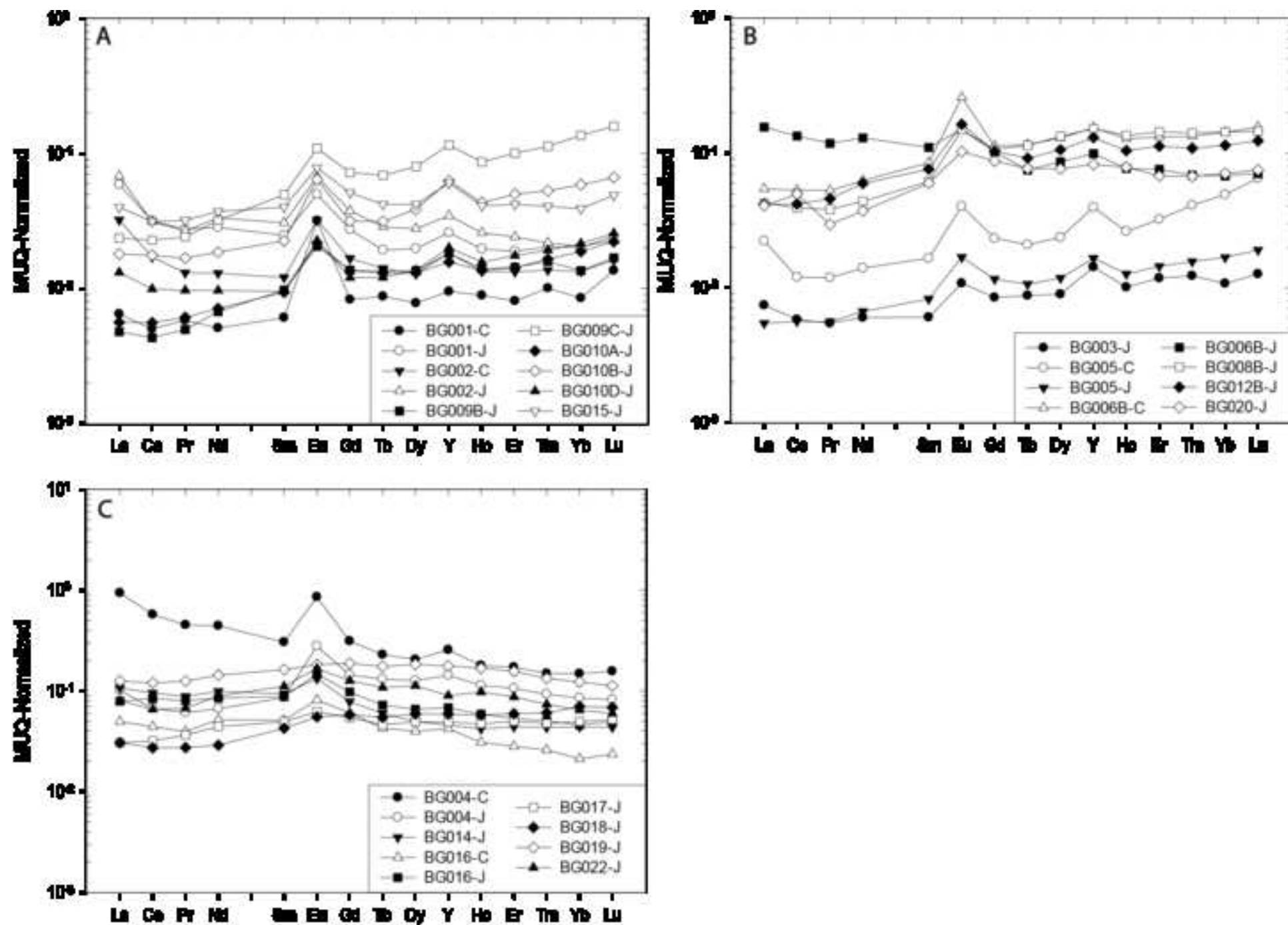
ACCEPTED MANUSCRIPT

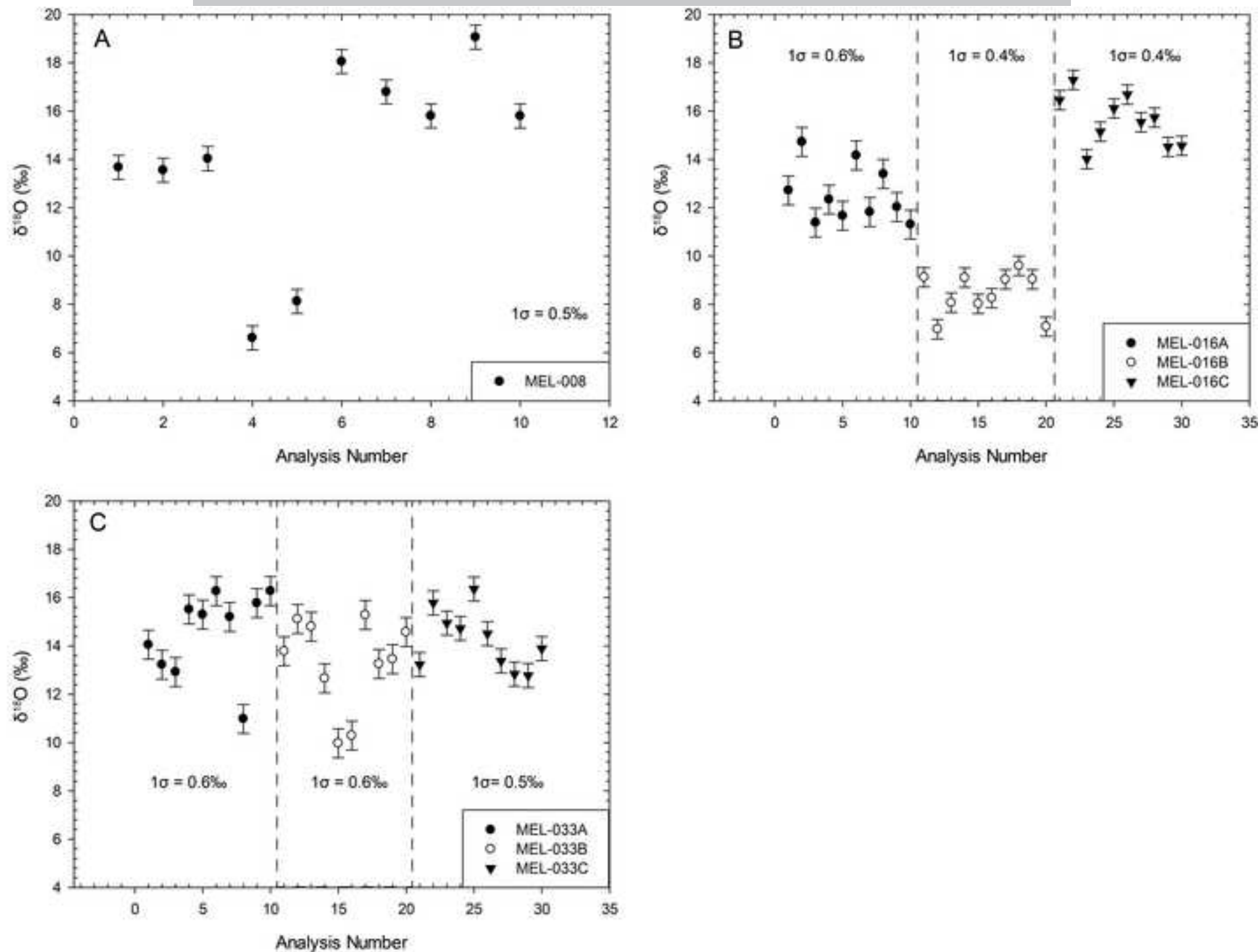












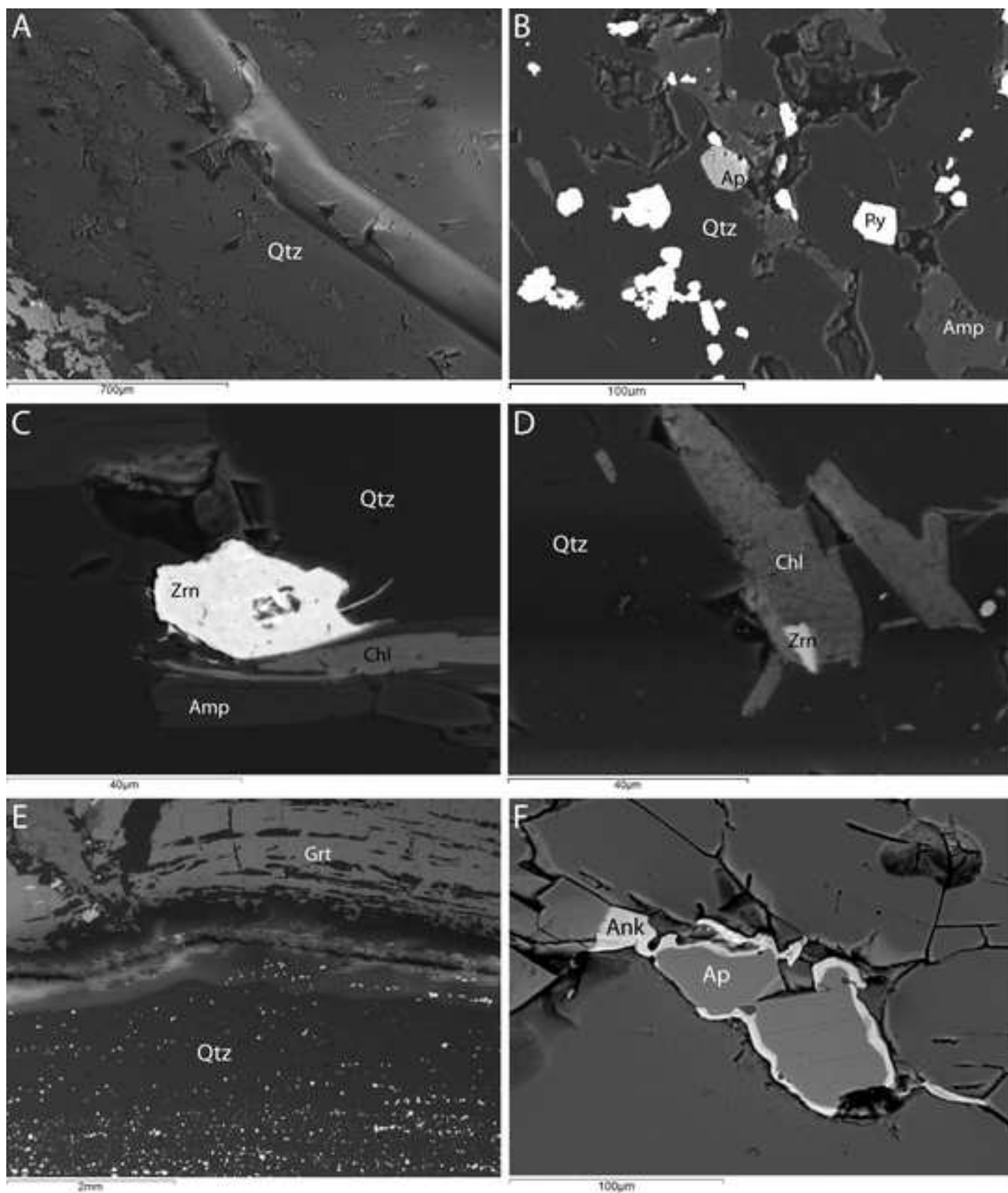
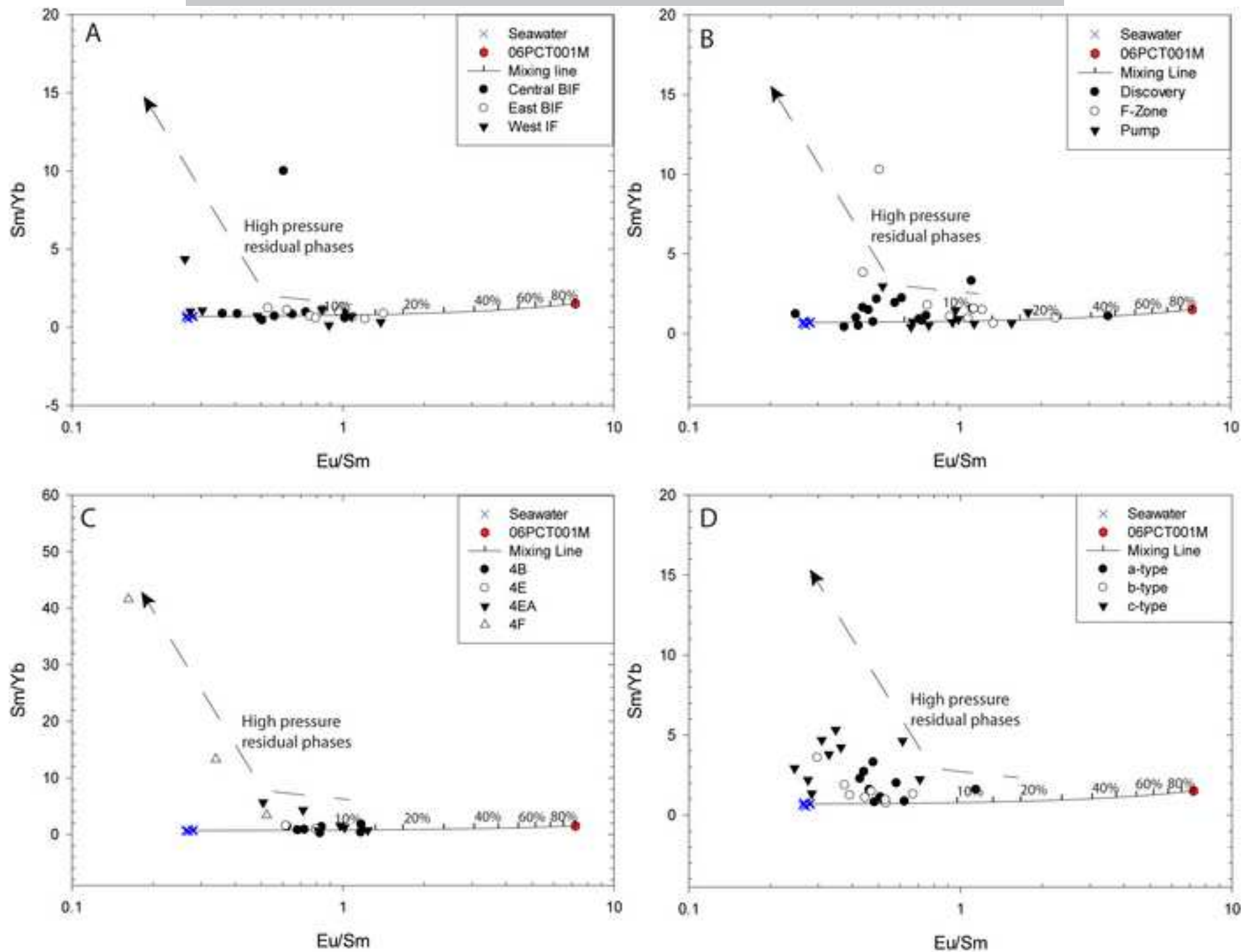
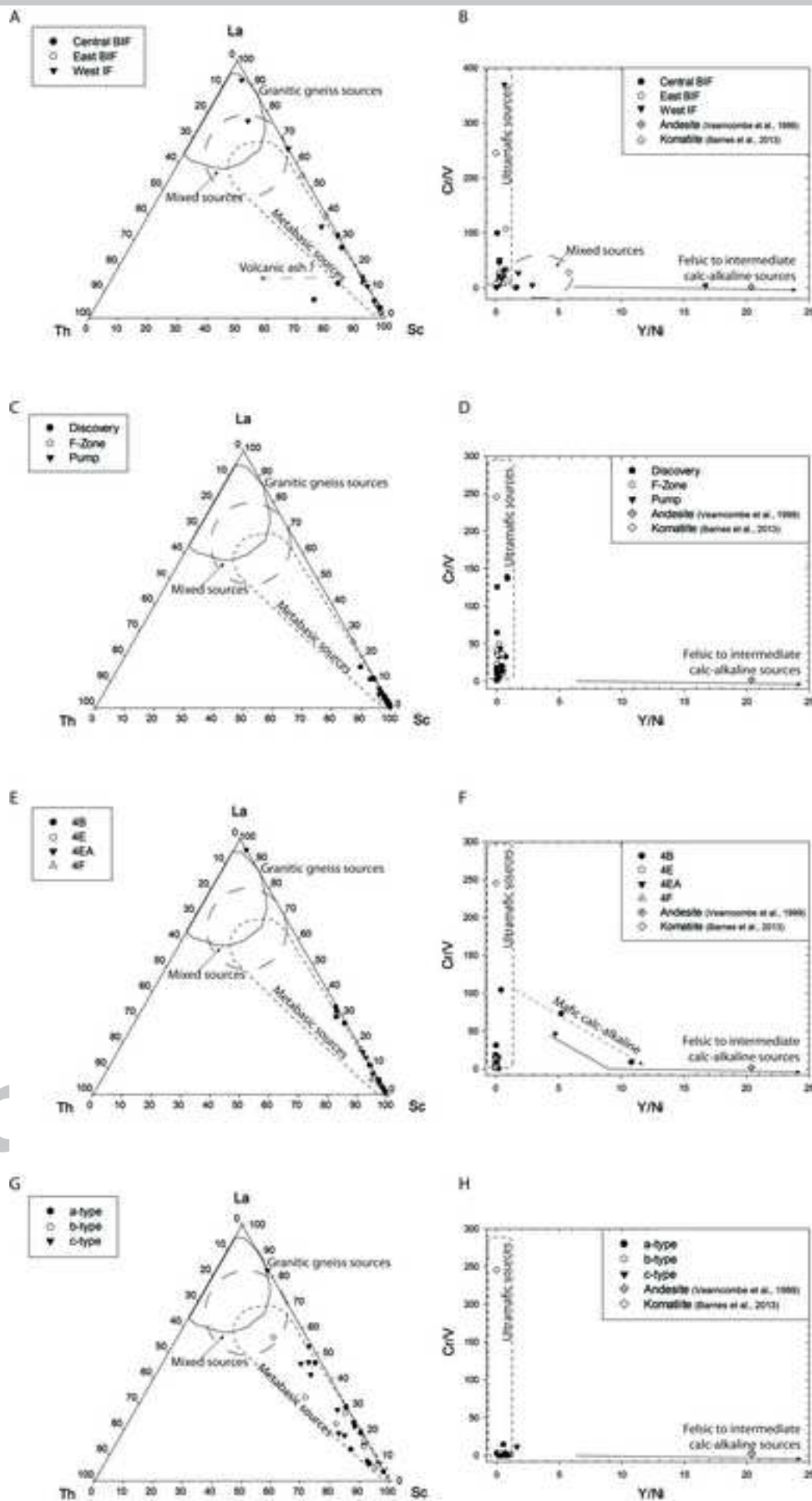
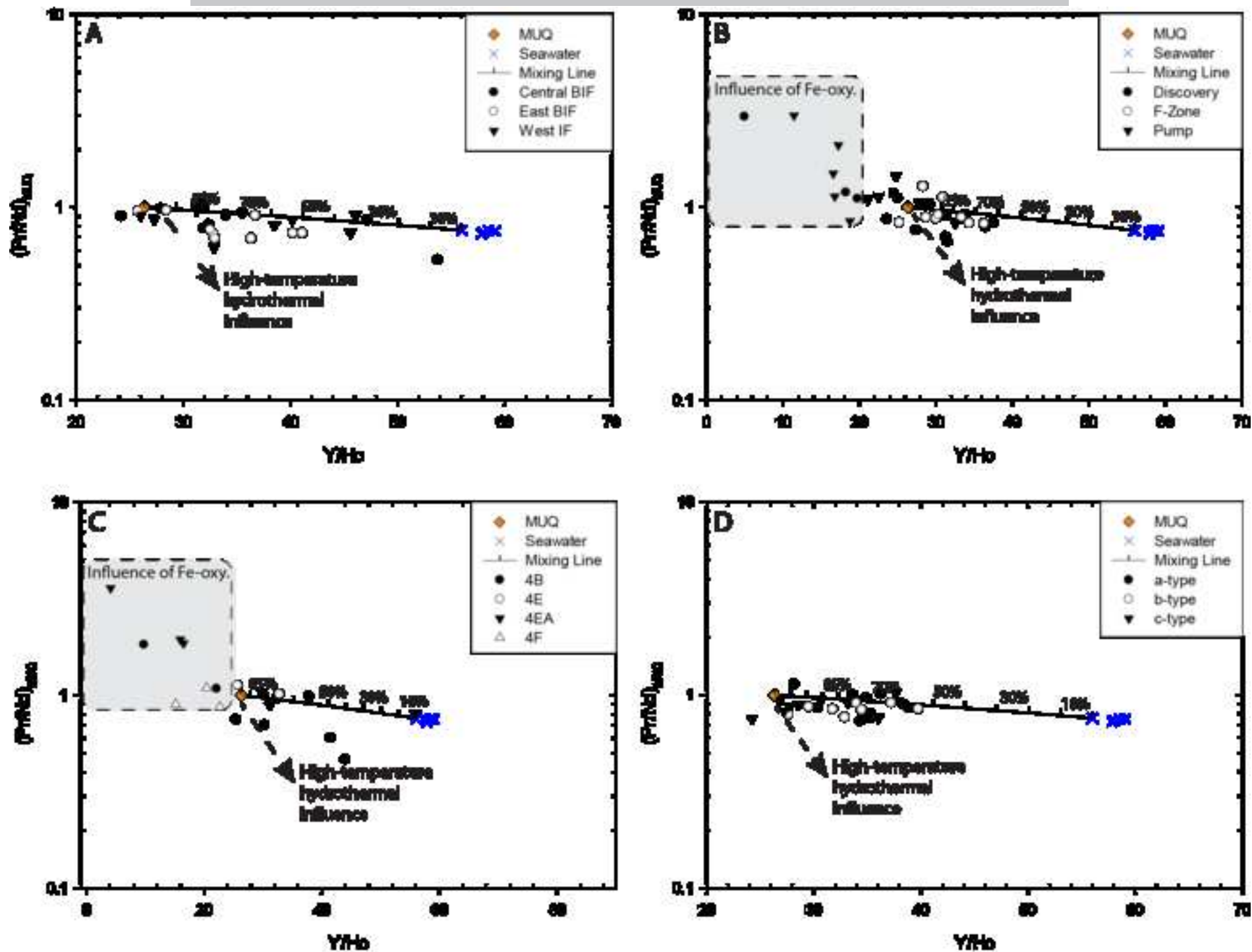
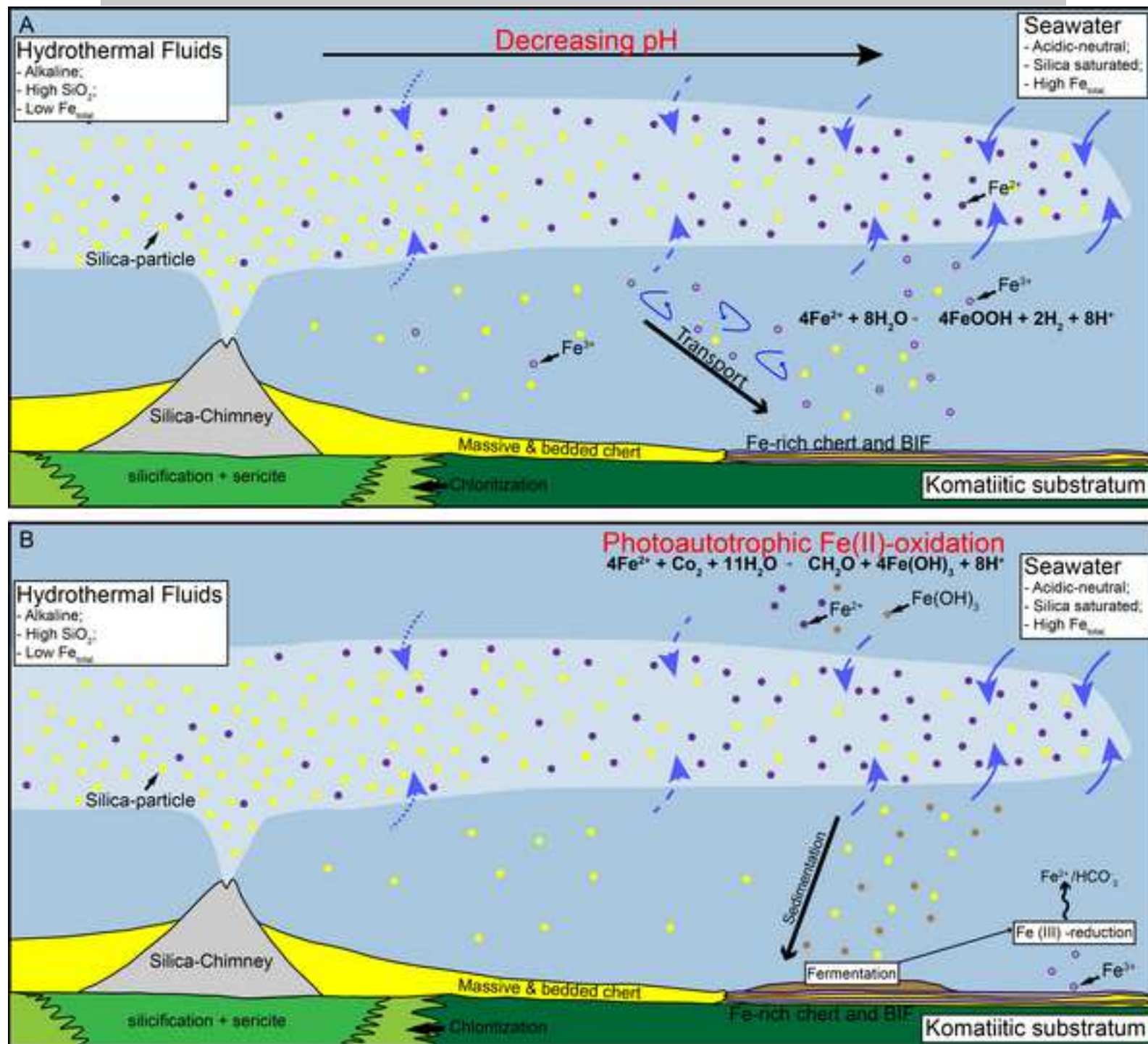


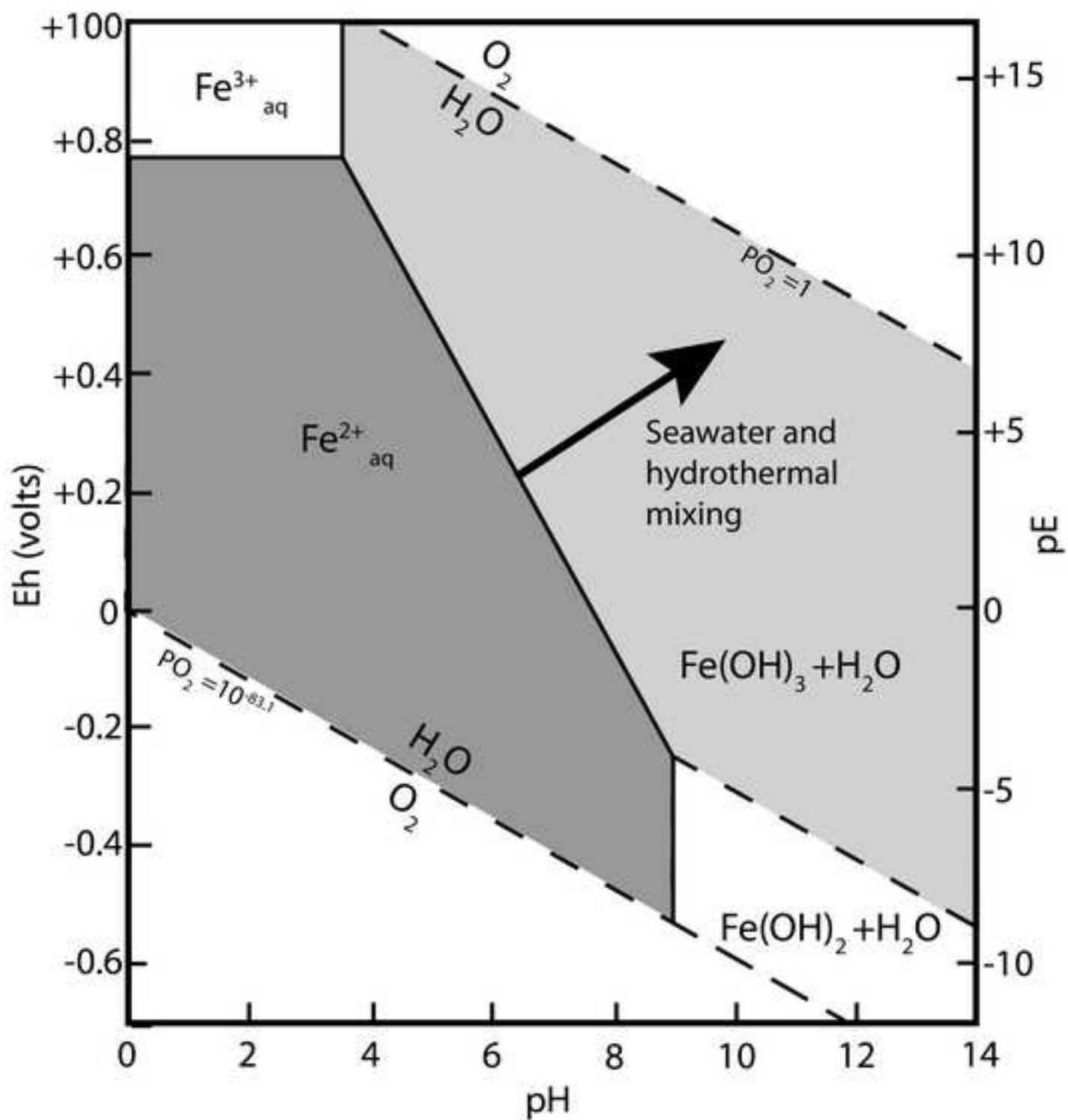
Figure 9

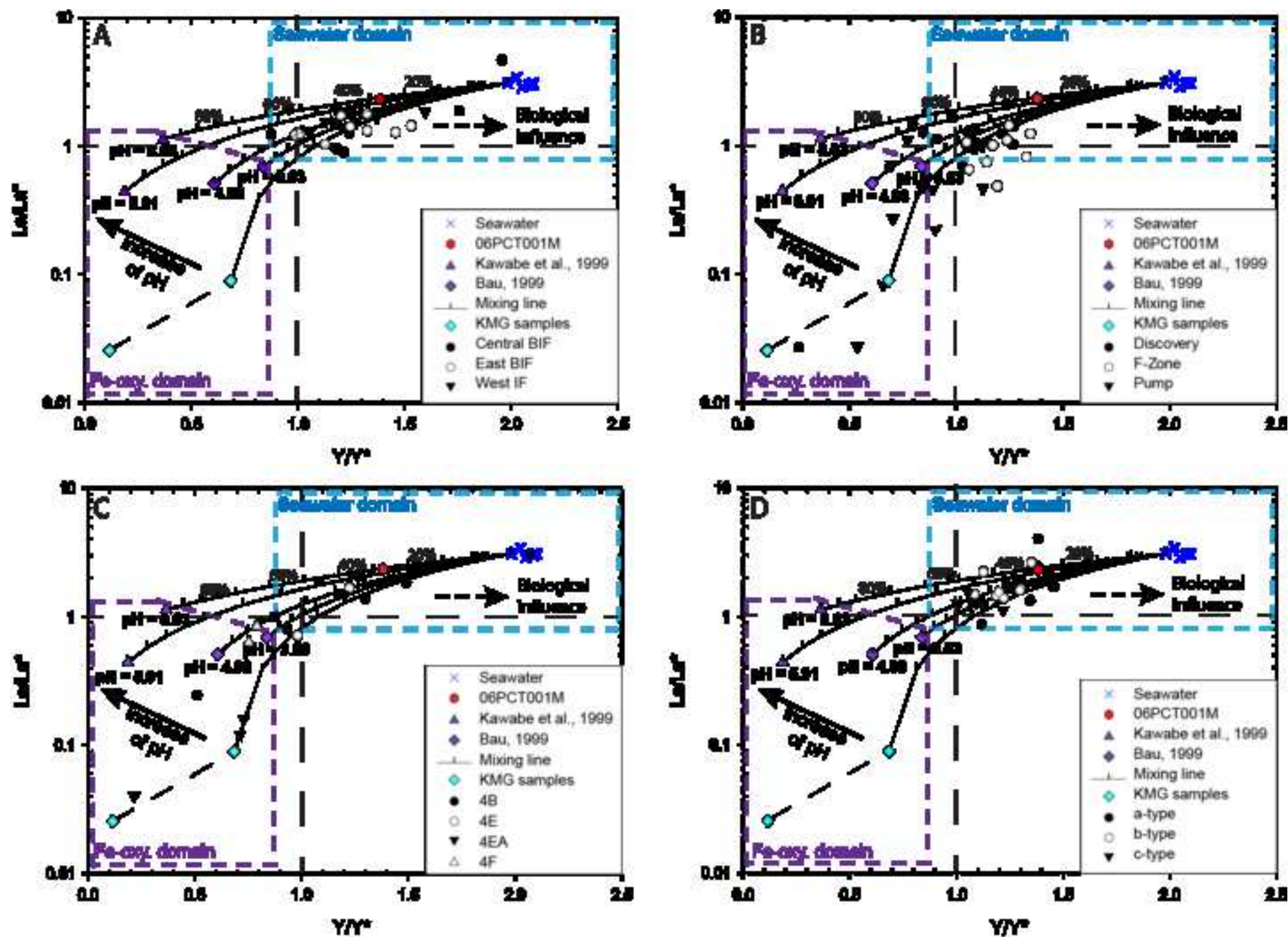


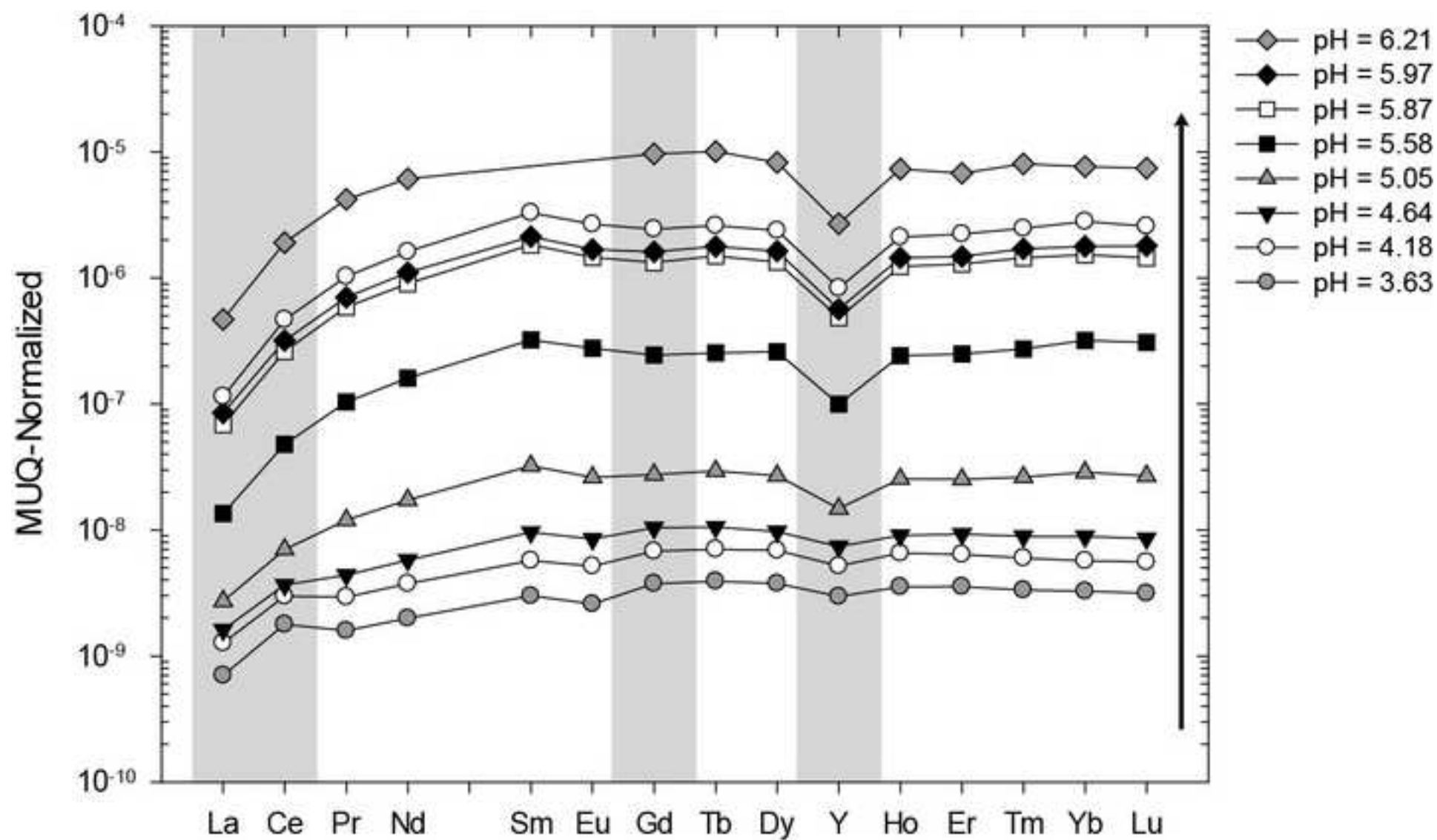












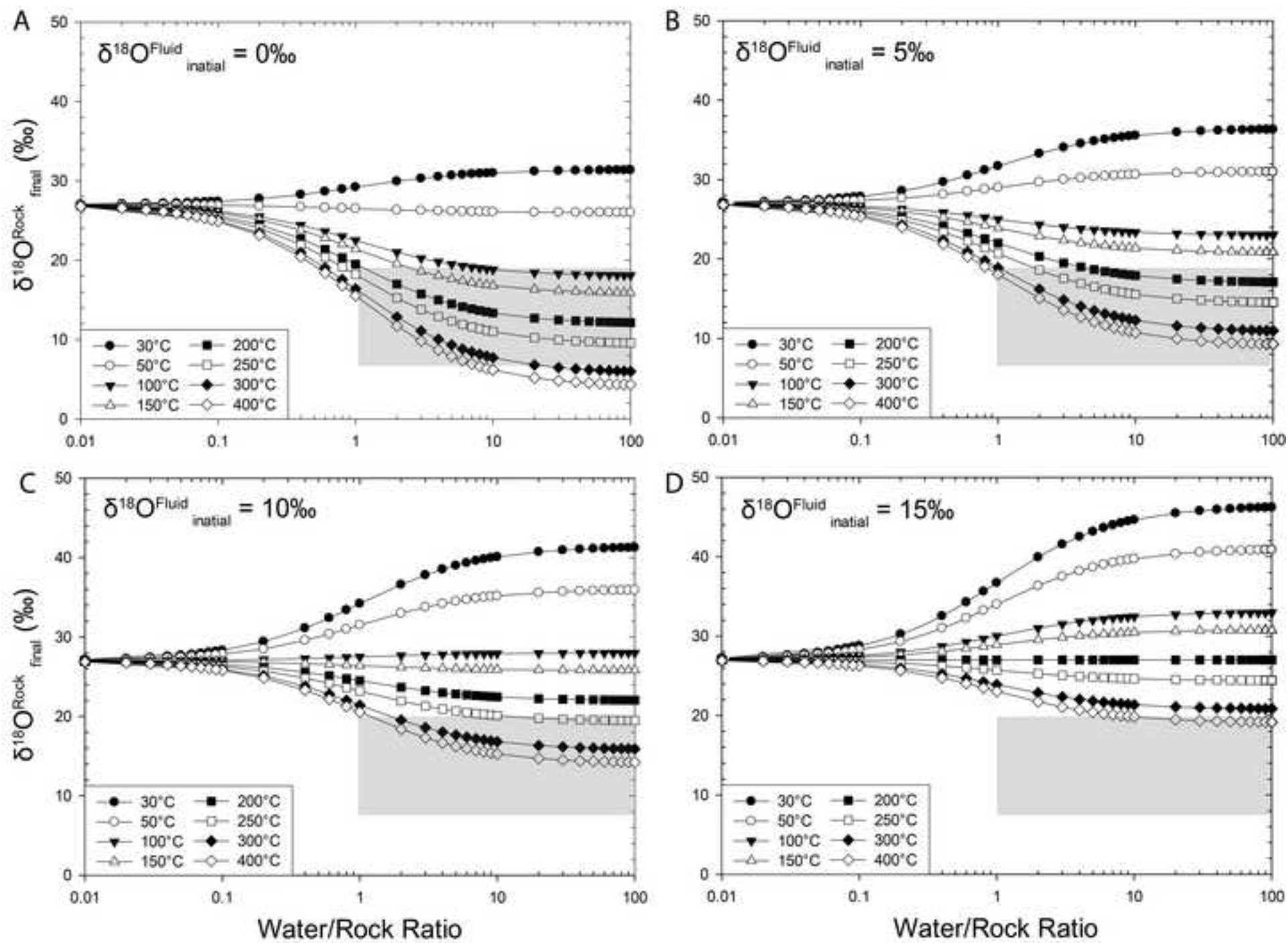


Table Caption

Table 1. Abundances of elements and REE+Y for samples from the Meadowbank gold deposit.

Table 2. Abundances of elements and REE+Y for samples from the Meliadine gold district.

Table 3. Abundances of elements and REE+Y for samples from the Musselwhite gold deposit.

Table 4. Abundances of elements and REE+Y for samples from the Beardmore Geraldton gold district.

Table 5. Oxygen isotope compositions as per mil (‰) deviations from the Vienna Standard Mean Ocean Water (V-SMOW) of chert samples determined by ion microprobe from the Meliadine gold district.

Table 6. Abundances of elements and REE+Y for KMG samples from the Meliadine gold district.

Highlights

► REE + Y geochemistry of chert in Algoma-type BIF. ► Oxygen isotope composition of chert in Algoma-type BIF. ► Documentation of seawater, hydrothermal and Fe-oxyhydroxide signatures, with some crustal contamination. ► Documentation of post-depositional events on primary trace element signature.

ACCEPTED MANUSCRIPT